Numerical Modeling of Anchoring System for Marine Renewable Energy Sources in Clay Soils

February 28, 2023

TEAMER RFTS-4 Final Report

Charles Aubeny, PhD, PE
Husham Al Janabi, PhD
Junho Lee, PhD
Ahmed Radwan

Texas A&M University

Table of Contents

Figures

Tables

1. Introduction

Triton Systems is working toward lowering the levelized the cost of energy (LCOE) for the marine renewable energy (MRE) industry by focusing on one of the costliest portions of offshore energy field development: anchoring.

Triton's Helical Anchor Group Installation System (HAGIS) is designed to target soil and mooring conditions that current anchors fail in. Specifically, HAGIS is being developed to provide an anchoring solution for high-uplift mooring conditions. Triton's collaboration with Texas A&M University (TAMU) and the Offshore Technology Research Center (OTRC) is focused on developing a viable new anchoring solution for the MRE industry. This anchor will accurately secure MRE converters to the seafloor without a need for vast amounts of mooring components in the water and on the seafloor that can cause severe environmental and fishing industry impacts. OTRC, with its thirty-plus years of mooring and anchoring testing expertise, will provide Triton Systems with soil-structure computational and numerical modeling capabilities to analyze and develop an anchor in realistic soil profiles and loading conditions.

Specifically, this test will quantify the effects on holding capacity in normally consolidated clay profiles of four issues: monotonic load capacity of the combined helical piles and skirt system, installation disturbance effects and corresponding set-up times, anchor performance under cyclic loading, and creep effects on HAGIS.

2. Role and Responsibilities of Project Participants

The following team members support the project:

2.1 Triton Systems Team:

Zachary Miller is the Principal Investigator and Project Manager of Triton's anchor system. He is the Triton Systems primary point of contact supervising the testing and overall anchor development.

Nathan Krohn, is an Installation Engineer with Triton supporting the development and testing of the anchor system.

Paul Sauco, PhD, PE, is a Geotechnical Engineer with Triton supporting the development and testing of the anchor system.

2.2 TAMU OTRC Team:

Charles Aubeny, PhD, PE, is the Lead Researcher with Texas A&M University who is supervising this project.

Husham Al Janabi, PhD, a post-doctoral researcher, is conducting finite element simulations and interpreting the findings.

Junho Lee, PhD, a post-doctoral researcher, is conducting finite element simulations and interpreting the findings.

Ahmed Radwan, a doctoral student, is conducting finite element simulations and interpreting the findings.

2.3 Applicant Responsibilities and Tasks Performed

Triton leads the anchor analyses by providing the desired areas of analysis support needed (Section 3), specific anchor dimensions, loading conditions, and performance expectations as well as any other relevant information to support each test.

2.4 Network Facility Responsibilities and Tasks Performed

TAMU OTRC provides experienced personnel and the testing facility with equipment necessary to conduct the analysis as described in Section 4 and Section 6 to meet the objectives defined in Section 3.

3. Project Objectives

The technical objectives are to quantify the effects on holding capacity in clay profiles of four issues: monotonic load capacity of the combined helical piles and skirt system, installation disturbance effects and corresponding set-up times, anchor performance under cyclic loading, and creep effects on HAGIS. Meeting these objectives will prove whether the anchor is able to withstand the variety of peak and time-dependent mooring loads that are required to operate in the offshore environment.

3.1 Monotonic Load Capacity:

The monotonic load capacity studies investigate and considers the effects of soil heterogeneity, soil-anchor friction, gapping at the soil-anchor interface of the skirt, pad-eye location, load inclination angle ranging from purely horizontal to purely vertical, system level installation angle effects, and interaction effects on group capacity of the plate anchors. A key issue in the monotonic load capacity evaluation is accurately characterizing the effects of anchor installation disturbance.

Two disturbance categories will be considered in this study: soil remolding from helical anchor installation and reduced shear resistance at the soil-anchor interface.

3.2 Installation and its Effects on Setup/Consolidation:

Installation of helical anchors will create vertical columns of disturbed soil above the anchors. Immediately after insertion, the soil strength in these columns will approach the soil remolded strength, usually 25-35% of intact strength. Reconsolidation will produce some strength recovery, which this research will address at two levels. The first will quantify the strength recovery using a hydromechanical model to simulate reconsolidation in the zone of disturbance. The second level will assess the effect of the disturbed soil columns on anchor performance, with particular focus on the implications of disturbed soil columns on anchor capacity for various load inclination angles. Numerical modeling of strength recovery after remolding is extremely challenging, so this study should be regarded as a first-order estimate that should be validated by follow-up experimental investigations.

Friction at the soil-anchor interface results from remolding and reconsolidation similar to that described for the disturbance due to helical anchor insertion but with important differences. An extensive database of friction coefficients exists for piles and caissons. The research team will consider using empirically derived friction values directly into numerical models as the most reliable approach to simulating soil anchor interface friction.

3.3 Cyclic Effects

A critical concern is the potential upward ratcheting of plates during cycling, which can lead to losses of embedment and uplift resistance. Analysis of this process requires a constitutive model capable of simulating yield beneath the ultimate stress state, described later. Previous work on this problem by TAMU found cumulative deformations to be highly sensitive to the adhesion factor

and yield stress. This work involved calibrating simulations to experimental measurements to back-calculate the yield stress. Findings from these studies will be applied to the proposed work to provide realistic yield stress values as inputs into the numerical models.

3.4 Creep Effects

Under loading conditions where mean uplift loads exceed zero, creep effects are of concern in soft clays. Creep in uplift causes loss of embedment and load resistance, so attention to this issue is warranted. For mooring systems involving sustained vertical loading, maintaining stress levels below the level at which significant creep movement initiates is a major design consideration.

4. Test Facility, Equipment, Software, and Technical Expertise

Relevant capabilities of the facility that was used to achieve the objectives of the project include the following:

- The computer code ABAQUS was used for most of the numerical investigations conducted in this investigation. This code has capabilities for both purely mechanical analyses as well as for coupled hydromechanical analyses. The former will be utilized for studies of anchor performance under monotonic and cyclic loading, while the latter will be utilized to investigate the recovery of soil resistance following anchor installation disturbance. ABAQUS also has an extensive material library, featuring classical von Mises and Mohr-Coulomb yield models, a cyclic loading model, a critical state soil mechanics model, and creep models. OTRC also possesses a number of in-house plastic limit analyses, which will be used to provide benchmark solutions for ultimate anchor capacity that will be used to verify convergence and accuracy of the finite element models.

- Dr. Charles Aubeny has 22 years of experience in supervising and performing numerical investigations into the performance of both plate and tubular anchors. His research and consulting experience includes investigations on ultimate monotonic load capacity under combined (axial-lateral-moment) loading conditions, cumulative deformations and/or progressive weakening under cyclic loading, coupled analysis of consolidation under sustained loading, prediction of installation disturbance and post-installation setup, and analysis of rate-dependency effects.

- Dr. Husham Al Janabi conducted doctoral research at Texas A&M University that included cyclic modeling of anchors using the program Abaqus, laboratory model tests on cyclically loaded anchors, and characterizing remolded soil strength and thixotropic strength gain in clays. This experience directly relates to two major focus areas in this research: plate and caisson performance under cyclic loading and simulating soil disturbance effects.

- Dr. Junho Lee performed his doctoral research on the behavior of marine infrastructure, including the performance of tubular and plate anchors in clays under complex loading conditions. He is actively involved in a research project in which his numerical simulations are supporting an experimental centrifuge test program conducted by a partner institution, which involves monotonic and cyclic testing of an anchor embedded in a clay testbed. He has had prior experience in his Master's research on characterizing strain-dependent soil behavior for dynamic analysis modeling. Therefore, his familiarity with observed anchor behavior will provide a valuable basis for assessing the reliability of the finite element simulations.

- Ahmed Radwan is a doctoral student at Texas A&M who focuses on marine soil-foundation interactions using numerical simulations. During his Master's thesis, he studied

the soil interaction for the marine foundation with a type of spud-can under a vertical pushing load, which was for investigating the stability of the installation process of the JACK-UP marine rig using numerical simulations. Due to his experience, he can conduct the numerical modeling required for the current study.

5. Test or Analysis Article Description

The HAGIS anchor is intended to provide a better, lower cost anchoring solution for marine energy technologies.

MRE technologies present particular challenges to anchoring and mooring systems due to the nature of how they function. Since these technologies extract energy from highly energetic areas in the ocean, this transmits large and highly cyclic loads to the anchors. Further adding to these challenges, MRE technologies need to be developed in large arrays to generate competitive levels of energy. If drag anchors are used, these arrays would lead to a spider web of mooring lines in the water and on the seabed severely impacting both the local environment and fisheries. When high vertical uplift capacity anchors are used such as driven piles, the main problems are related to the increased installation complexity and environmental hazards as well as increased manufacturing costs. A proven HAGIS anchoring method eliminates both of these risks by providing an anchor with high uplift capacity, nearly silent installation, and an option for mooring with little interaction with the seafloor. Figure 1 illustrates the HAGIS anchor, comprising a skirt surface, connected to deep helical plate anchors by cables, the cable plate system denoted as a helical pile. Uplift resistance derives almost entirely from the plates, with side friction along the cables being considered negligible.

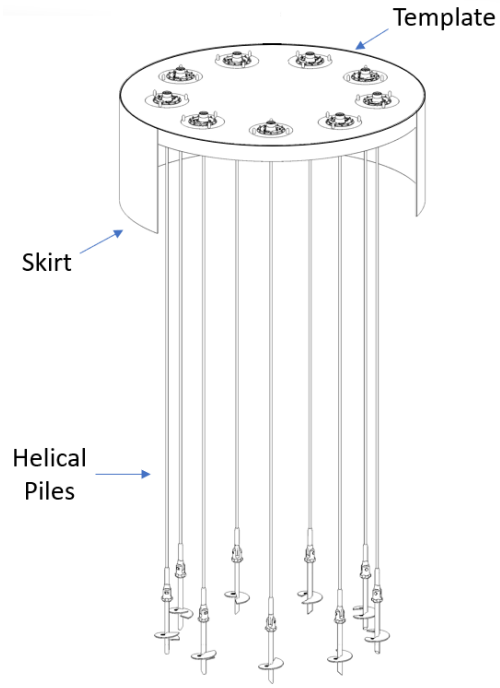

Figure 1: HAGIS Anchor Diagram

The amount, length, and diameter of helical piles as well as the dimensions of the skirt and template can be scaled to provide a solution for any size MRE technology with any type of mooring system. As such, a range of lengths and quantities of helical piles at varied spacing with multiple diameters and skirt lengths will be considered during this study. These simulations will provide Triton the ability to quantify the appropriate parameters to optimize the anchor for its intended applications.

6. Constitutive models

This study employs different constitutive models according to the problem under consideration. Table 1 indicate the summary of modeling methodologies associated with the constitutive models. A kinematic hardening model is used for simulating HAGIS performance under undrained monotonic and cyclic loading conditions. Two methods are used to simulate the anchor plate-cable portion of the HAGIS. In some cases, the cable-plate assemblies are modeled using the non-linear

spring feature offered in ABAQUS. In other cases, the plates are modeled as a rigid disk embedded in the soil continuum, connected to the skirt by cables modeled as linear spring elements. Further details on modeling the plates and cables are contained later sections of this report. The creep studies utilized the viscoelastic model offered in the ABAQUS material library.

Table 1: Modeling methodologies in this study

Process	FE Model Dimension	Procedure	Soil Model
Monotonic loading (Skirt-plate)	3D	Static	Linear elastic perfectly plastic Spring element
Single plate loading (develop springs)	2D Axisymmetric	Static	Linear elastic perfectly plastic
Interference on plate groups	3D/Cyclic symmetry 3D	Static	Linear elastic perfectly plastic
Cyclic loading	3D	Static	Kinematic hardening Spring element
Creep	2D Axisymmetric	Viscoelastic	Viscoelastic
Consolidation/Setup	2D Axisymmetric	Consolidation	MCC model: Critical state and porous elasticity

6.1 Linearly elastic-perfectly plastic soil model

In order to estimate the relationship between load and displacement for the helical anchor, the FE model assumes linearly elastic-perfectly behavior below a Tresca yield surface and associated flow at yield. A Poisson's ratio μ=0.49 approximates undrained loading. As the anchor is assumed to be deeply embedded and no gapping occurs, the FE-computed values are not affected by soil weight and the soil can be assumed to be weightless. Full bonding was assumed at the soil–anchor interface. Murff et al. (2005) showed that the adhesion factor had a slight effect on the ultimate

capacity of plate anchor oriented normally to the loading direction. A series of the FE analyses in the present study yielded results consistent with this trend, with the change in a bearing factor over a range of adhesion α=0.4–1.0 never exceeding 7%. Given the insensitivity of computed bearing factors to changes in α, a fully rough bonding at the soil–anchor interface, α=1, was assumed in the parametric studies. Since the focus of this study is on ultimate load capacity, and since the elastic behavior does not influence the ultimate load capacity (Chen 1975), stress–strain behavior was assumed as linear with Young's modulus E/s_u=150 or 500.

6.2 Kinematic hardening model (for monotonic and cyclic study)

The model used in this study aims only to simulate purely undrained behavior; as such, pore-pressure dissipation is not simulated. However, undrained behavior is considered a reasonable simplification first approximation for fine-grained soil subjected to rapid cyclic loading relative to the relatively short duration of a storm event.

Uniaxial strength σ_{max} controls the size of the limit state surface. For a Von Mises yield criterion, σ_{max} relates to undrained shear strength s_u by (Eq. 1).

$$\sigma_{max} = \sqrt{3}\, s_u \qquad \text{(Eq. 1)}$$

The evolution law for this model (Simulia, 2014) consists of two hardening components: kinematic and isotropic. The kinematic hardening component describes the translation of the yield surface in stress space through the backstress parameter α_b. The isotropic hardening component describes the change of the equivalent stress defining the size of the yield surface, σ^o, remains constant, $\sigma^o = \sigma_o$, where σ_o is the equivalent stress defining the size of the yield surface at zero plastic strain (Figure 2). The FE analysis in this study invokes only the kinematic hardening capabilities of the model. The evolution of stresses is defined as

$$\sigma = \sigma_o + \alpha_b \quad \text{(Eq. 2)}$$

where α_b is the backstress, which determines the kinematic evolution of the yield surface in the stress space.

The yield surface of the kinematic hardening model is defined as

$$F = f(\sigma - \alpha_b) - \sigma_0 = 0 \quad \text{(Eq. 3)}$$

where $= f(\sigma - \alpha_b)$ is the equivalent Mises stress with respect to the backstress α_b.

The kinematic hardening models assume associated plastic flow:

$$\dot{\varepsilon}^{pl} = \dot{\bar{\varepsilon}}^{pl} \frac{\partial F}{\partial \sigma} \quad \text{(Eq. 4)}$$

where $\dot{\varepsilon}^{pl}$ (defines the isotropic hardening component of the model) is the rate of plastic flow and $\dot{\bar{\varepsilon}}^{pl}$ is the equivalent plastic strain rate.

The evolution of the kinematic component of the yield stress is described by the expression.

$$\dot{\alpha}_b = C \frac{1}{\sigma_\circ} (\sigma - \alpha_b) \dot{\bar{\varepsilon}}^{pl} - \gamma \alpha_b \dot{\bar{\varepsilon}}^{pl} \quad \text{(Eq. 5)}$$

where C = initial kinematic hardening modulus [$C = E$] (Anastasopoulos et al. 2011) and γ is a parameter determining the rate of decrease of the kinematic hardening with increasing plastic deformation. Since $\sigma_{max} = C/\gamma + \sigma_o$, γ can be found using (Eq. 6) (Gerolymos et al. 2005; Anastasopoulos et al. 2011).

$$\gamma = \frac{C}{\sqrt{3} s_u - \sigma_\circ} \quad \text{(Eq. 6)}$$

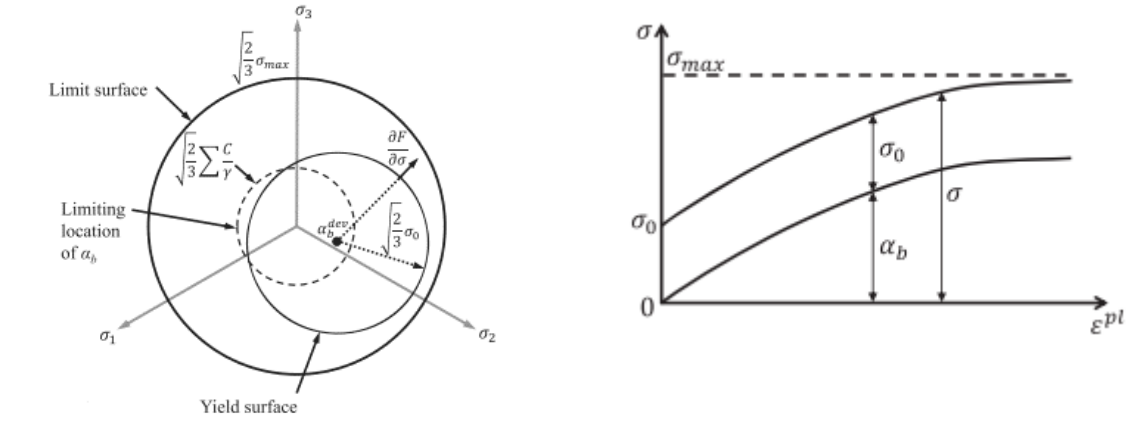

(a) (b)

Figure 2: Hardening model (Simulia, 2014): (a) yield surface; (b) stress-strain behavior.

The simulations conducted in this study are intended to represent typical normally consolidated clay conditions, as opposed to providing site-specific predictions of HAGIS anchor performance, parameter selection is based on previous studies of cyclic loading performed by research team. The form of the hardening model used in this study requires four model input parameters: maximum stress σ_{max}, Young's modulus E, Poisson's ratio μ and a yield stress σ_0. The maximum stress is selected to match the undrained shear strength at the depth level under consideration. Poisson's ratio is taken as about 0.5 to replicate undrained loading conditions. The Young's modulus and yield stress values are selected based on previous studies matching finite element simulations to single-gravity (Al-Janabi and Aubeny, 2022) and centrifuge tests (Randolph et al., 2009.) Specific values selected for the simulations are given in Section 9.4 of this report. Future studies are planned to determine model input parameters appropriate to the HAGIS based on experimental single-gravity test basin studies.

6.3 Spring elements

The SPRINGA element is available in both Abaqus/Standard and Abaqus/Explicit. SPRINGA acts between two nodes, with its line of action being the line joining the two nodes, so that this line of action can rotate in large-displacement analysis. The spring behavior can be linear or nonlinear in any of the spring elements in Abaqus.

A SPRINGA element introduces a stiffness between two degrees of freedom without introducing an associated mass. In an explicit dynamic procedure this represents an unconditionally unstable element. The nodes to which the spring is attached must have some mass contribution from adjacent elements; if this condition is not satisfied, Abaqus/Explicit will issue an error message. If the spring is not too stiff (relative to the stiffness of the adjacent elements), the stable time increment determined by the explicit dynamics procedure will suffice to ensure stability of the calculations.

For geometrically linear analysis the relative displacement is measured along the direction of the SPRINGA element in the reference configuration:

$$\Delta u = \frac{(\mathbf{X}^1 - \mathbf{X}^2)}{\sqrt{(\mathbf{X}^1 - \mathbf{X}^2) \cdot (\mathbf{X}^1 - \mathbf{X}^2)}} \cdot (\mathbf{u}^1 - \mathbf{u}^2), \qquad \text{(Eq. 7)}$$

where $\mathbf{X}^1$ is the reference position of the first node of the spring and $\mathbf{X}^2$ is the reference position of its second node.

For geometrically nonlinear analysis the relative displacement across a SPRINGA element is the change in length in the spring between the initial and the current configuration:

$$\Delta u = l - l_0, \qquad \text{(Eq. 8)}$$

where $l = \sqrt{(\mathbf{x}^1 - \mathbf{x}^2) \cdot (\mathbf{x}^1 - \mathbf{x}^2)}$ is the current length of the spring and l_0 is the value of l in the initial configuration. Here $\mathbf{x}^1$ and $\mathbf{x}^2$ are the current positions of the nodes of the spring.

In either case the force in a SPRINGA element is positive in tension.

6.4 Viscoelastic model (creep test)

The linear viscoelastic system may consist of simple models composed of springs and dashpots. The basic arrangement of these components (spring and dashpot) in the Maxwell, Kelvin-Voigt, and three-parameter models along with the constitutive stress –strain relationship is presented in Figure 3.a. The three-parameter model has a Maxwell element attached in parallel with a spring element. Prony series is defined as the mathematical expression representing n Maxwell elements arranged in series as presented in Figure 3.b. This arrangement of Maxwell elements in parallel with a spring element represents a general model for linear viscoelastic stress–strain behavior for nonhomogeneous solids.

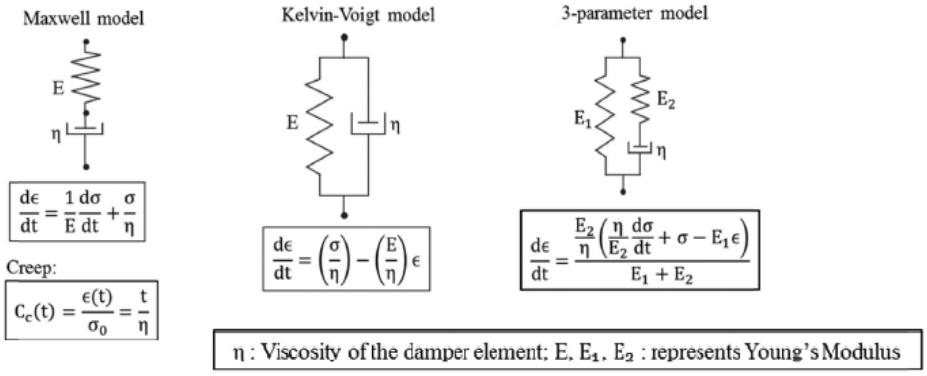

(a) Basic lumped parameter models for soil

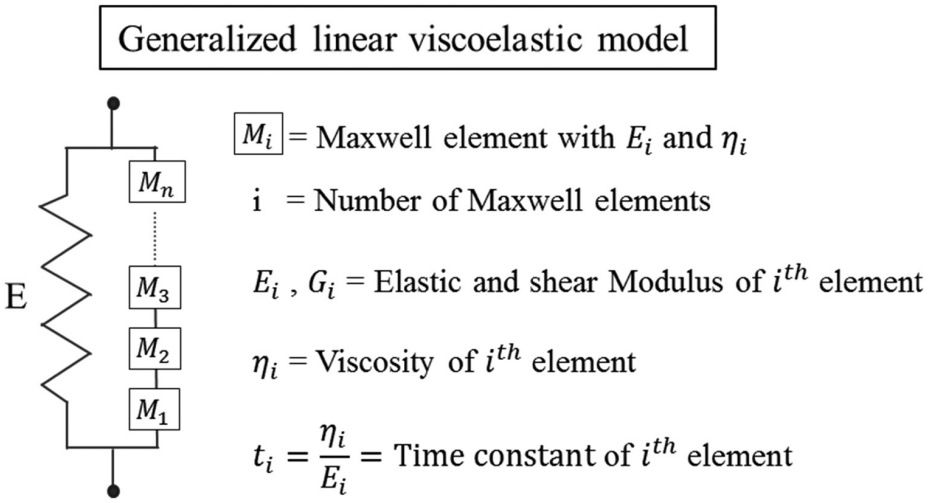

b) generalized linear viscoelastic lumped parameter model.

Figure 3: (a) Basic lumped parameter models for soil; and (b) generalized linear viscoelastic lumped parameter model.

In terms of the shear modulus of soil, the shear relaxation modulus (G_R) can be expressed as

$$G_R(t) = G + \sum_{i=1}^{n} G_i \cdot (e)^{-t/t_i} \qquad \text{(Eq. 9)}$$

$$\Rightarrow \frac{G_R(t)}{G_0} = \frac{G_\infty}{G_0} + \sum_{i=1}^{n} \frac{G_i}{G_0} \cdot (e)^{-t/t_i} \quad \text{where} \begin{cases} G_\infty = \lim_{t \to \infty} G_R(t) \\ G_0 = G_R(t=0) \end{cases} \qquad \text{(Eq. 10)}$$

$$\Rightarrow g_R(t) = \left(1 - \sum_{i=1}^{n} g_i\right) + \sum_{i=1}^{n} g_i \cdot (e)^{-t/t_i}$$

$$\Rightarrow g_R(t) = 1 - \sum_{i=1}^{n} g_i \cdot \left(1 - (e)^{-t/t_i}\right)$$

The shear modulus terms $G_R(t)$ and G_i are normalized with respect to G_0 and are represented by $G_R(t)$ and g_i, respectively, where $G_R(t)$ is defined as the normalized relaxation modulus. A general model with n number of Maxwell elements will have $(2n+1)$ unknown parameters (spring elements = $n + 1$; damping elements = n). After normalization, g_i and t_i are the material parameters that need to be determined.

The viscoelastic simulations require Prony series input parameters. This study adopts elastic and Prony series parameters derived by Swain and Ghosh (2019) from creep tests on a marine clay from the east coast of India. These authors provide parameter sets for 3, 5 and 7- parameter Prony series fits. The present study adopts a 7-parameter Prony series fit, as that provides the best match to experimental measurements. Specific input parameter values used in the creep studies are given in Section 6.5 of this report. Future studies are planned to determine model input parameters appropriate to the HAGIS based on experimental single-gravity test basin studies.

6.5 MCC model: Critical state and porous elasticity (for Consolidation Study)

In the current research work, the soil domain is a fully saturated, normally consolidated clay. Simulating the consolidation process requires an effective stress model. The Modified Cam Clay (MCC) in the ABAQUS material model library is appropriate for this purpose. MCC is a critical state model developed by Cambridge University's researchers (Roscoe and Burland, 1968; Schofield and Wroth, 1968). This model has been applied extensively to consolidation problems, with a study by Zi-hang and Zi-zhong (2013) being one example of its validation.

Basic stress measures for describing soil behavior using the MCC model are the mean effective stress (p') and a deviatoric stress measure (q). Eqs. 11 and 12 define these measures in terms of principal effective stresses σ_1', σ_2', σ_3'. (Wesley, Mike, Justin, John, and Graham, 2014.)

Volumetric behavior is described in terms of the void ratio (e) or incremental volumetric strain (Δv), defined by Eq. 13).

$$p' = \frac{1}{3}(\sigma_1' + \sigma_2' + \sigma_3') \quad \text{(Eq. 11)}$$

$$q = \sqrt{\left\{\frac{1}{2}[(\sigma_1' - \sigma_2')^2 + (\sigma_2' - \sigma_3')^2 + (\sigma_3' - \sigma_1')^2]\right\}} \quad \text{(Eq. 11122)}$$

$$\Delta v = -\frac{\Delta e}{1+e} \quad \text{(Eq. 133)}$$

The MCC model describes two aspects of soil behavior: inelastic behavior associated with post-yield loading and the elastic behavior within the yield surface. Description of the stress-strain relationships requires definition of four parameters (λ, κ, μ, and M). (I-Hsuan, and Chung, (2013). (λ) is the slope of the normal consolidation line (loading), (κ) is the slope of the swelling and recompression lines (unload-reload) on a semi-logarithmic scale (e-ln (p')). These two parameters can be calculated from the experimental measurements of the compression index (C_c) and the swelling index (C_s), which can be measured an isotropic consolidation test, and then by using the following equations: (Helwany, 2007)

$$\lambda = \frac{C_c}{\ln 10} = \frac{C_c}{2.3} \quad \text{(Eq. 14)}$$

$$\kappa = \frac{C_s}{\ln 10} = \frac{C_s}{2.3} \quad \text{(Eq. 15)}$$

A linear e-ln (p') relationship implies that the elastic bulk modulus is directly proportional to the current level of mean effective stress.

To define the position of the critical state line, the parameter (M) is used as a coefficient in the linear relationship between the deviatoric stress (q) and the mean effective stress (p'). (M) is a unique parameter for each soil and related mainly to the effective friction angle (φ') (Wood, 1990). Hence, it can be calculated as follows:

$$q = Mp' \quad \text{(Eq. 14)}$$

$$M = (6sin\phi')/(3 - sin\phi') \quad \text{(Eq. 15)}$$

Poisson's ratio μ is measured in a consolidated-drained triaxial shear test.

The MCC model assumes an elliptical yield surface in p'- q space. The right-hand side of the ellipse represents wet (contractive behavior) and the left-hand side represents dry (dilative behavior). The size of the yield surface is controlled by the pre-consolidation pressure, $P_c'=2\alpha$, where α is a state variable that increases with increasing plastic volumetric strain. Thus, the MCC model may be considered a density hardening model.

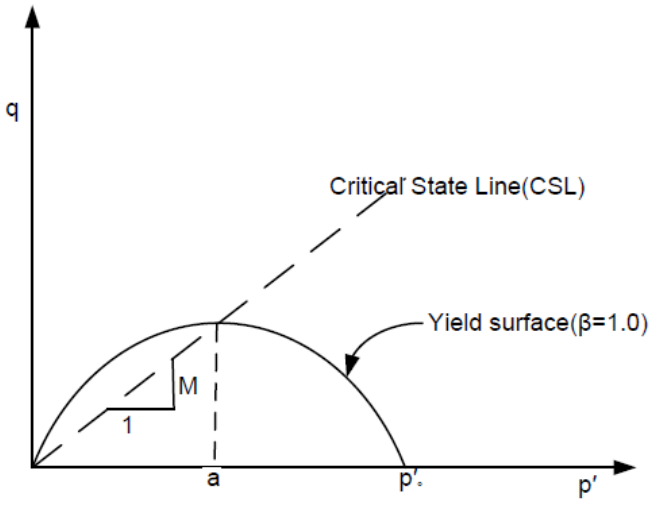

Figure 4: Modified Cam-Clay yield Surface. (Wesley, Mike, Justin, John, and Graham, 2014)

Roscoe and Burland (1968) developed the MCC constitutive model by defining the yield surface directly based on the pre-consolidation pressure which specifies the hardening condition of the soil structures (See. Eq. 18). And based the MCC model specifies the elastic behavior under the loading does not exceed the yield surface, once the loading exceeds the yield surface, the plasticity behavior would be captured until reaching the critical state line where the failure happens at the soil continues to distort without any noticeable effect on the shear stress.

$$\frac{q^2}{p'^2} + M^2\left(1 - \frac{p'_o}{p'}\right) = 0 \quad \text{(Eq. 16)}$$

ABAQUS has developed a more generalized equation (See. Eqs. 19 and 20) based on the equation of (MCC) by (Roscoe and Burland, 1968). This modified equation controls the yield surface shape by using the parameter β. This new parameter includes the effect of the yield surface shape parameter (β), and can be measured by Eq. 20 :

$$a = \frac{p'_0}{(1+\beta)} \quad \text{(Eq. 17)}$$

$$\frac{1}{\beta^2}\left(\frac{p'}{a} - 1\right)^2 + \left(\frac{q}{Ma}\right)^2 - 1 = 0 \quad \text{(Eq. 18)}$$

Since site-specific data are not available for this project, a default value $\beta = 1$ is used in this study. The current approach follows the yield surface that has the visualization of in three dimensions as shown in Figure 5.a., where the critical state surface appears as a cone principal effective stress ($\sigma'_1, \sigma'_2, \sigma'_3$) space.

The conventional MCC model typically uses a generalized von Mises approach to establish the yield criterion under combined shearing modes. This implies an unrealistically high (or even infinite) friction angle in the case of triaxial extension. To mitigate this problem, ABAQUS permits a modified shape of the yield surface in the π-plane by introducing a parameter K. This parameter distorts the shape the yield surface according to the magnitude of the third invariant of the stress tensor (Figure 5.b.). The possible range of K values varies from 0.778 to 1.0.

a)

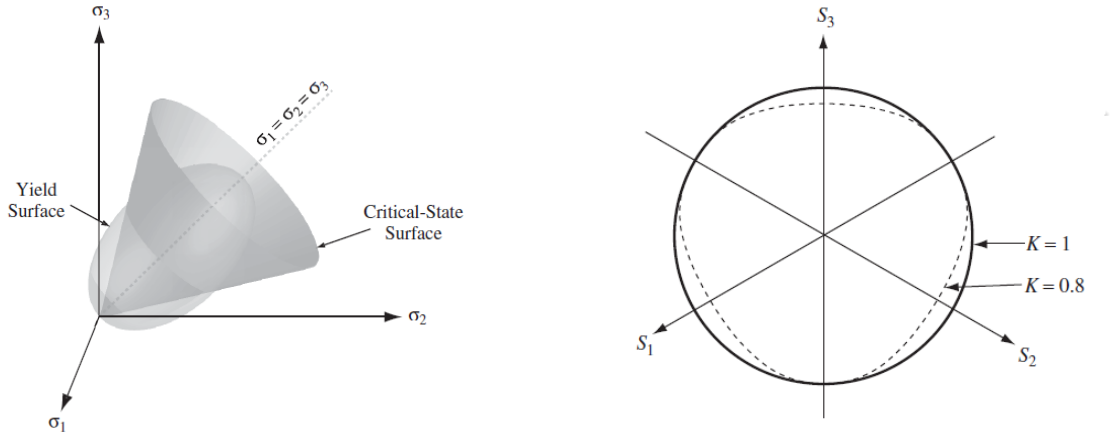

b)

Figure 5: a) Representing the yield surface and critical state surface in three-dimensions; and b) The Projection of the yield surface and critical state surface in three dimensions.
(Helwany, 2007)

Table 2 lists the model input parameters used in the installation disturbance consolidation study. These parameters correspond to typical parameters for normally consolidated clay. The parameter M is selected to provide a realistic value of undrained shear strength under direct simple shear loading, as opposed to a realistic drained friction angle. The inability to match both values is a basic limitation of the MCC formulation, which cannot model strength anisotropy. Since HAGIS load capacity under undrained loading conditions is a key focus of this study, the model parameter selection in this study prioritizes achieving realistic undrained shear strength values over other aspects of soil behavior, e.g., drained friction angle.

Table 2: The current study soil properties.

Parameters	**Values**
Effective specific unit weight (γ')(KN/m^3)	6.50
Earth pressure coefficient. (K_o)	0.55
Virgin compression coefficient. (λ)	0.22
Recompression coefficient. (κ)	0.044
Poisson's ratio. (μ)	0.35
Slope of critical state line. (M)	1.0
Ratio flow stress in triaxial compression to triaxial extension. (K)	0.8
Permeability. (k)(m/sec)	5.0e-7
Unit weight of water. (γ_w)(KN/m^3)	9.81
Void ratio.	1.0
Soil sensitivity in the remolded zone. (St)	3.0
Element type.	*CAX4P

7. Test Procedure

The matrix of numerical simulations is summarized in the tables below. The primary areas of focus are: (1) ultimate load capacity under monotonic loading, (2) cumulative deformation under cyclic loading, (3) creep movement under sustained loading, and (4) post-installation stress and degree of soil strength recovery following installation disturbance. Tables 3-5 show the test procedure for the monotonic, cyclic, and creep simulations, respectively.

The simulation matrix in Table 3 investigates the effects of plate spacing, number of plates, skirt aspect ratio and skirt diameter on ultimate load capacity under monotonic loading.

Table 3: Simulations for the monotonic loading.

Skirt length	Spacing details	Skirt OD (m)	no. of plates
1:0.5 (1/2 of OD) Figure 6.a.	Skirt only	5, 8, and 10	-
	3B	5	9
		8	30
		10	55
	Skirt only	6, 10, and 13	-
	4B	6	9
		10	31
		13	55
1:1 Figure 6.b.	Skirt only	5, 8, and 10	-
	3B	5	9
		8	30
		10	55
	Skirt only	6, 10, and 13	-
	4B	6	9
		10	31
		13	55

The simulation matrix in Table 4 investigates the effects of diameter-length ratio and the effects of embedded plates versus a skirt by itself.

Table 4: Simulations for cyclic loading.

Skirt length	Spacing details	Skirt OD (m)	no. of plates
1:0.5 (1/2 of OD)	Skirt only	5	-
	3B	5	9

Table 5 shows the four creep simulations performed, where the plate is embedded at a depth of 20 m in all cases, and sustained loads were applied at levels ranging from 25 to 100% of the allowable load, where the allowable load is taken as one-half of the ultimate load capacity.

Table 5: Simulations for creep simulations.

Simulation no.	Depth (m)	Sustained load kN
1	20	0.25 Fall
2		0.5 Fall
3		0.75 Fall
4		1.0 Fall

a) L=0.5D b) L=1.0

Figure 6: Different aspect ratio L=0.5D and L=1.0.

8. Finite Element Analysis

This study employs a linearly elastic-perfectly plastic model, nonlinear kinematic hardening model, and a viscoelastic model. The models are available in commercial FE (Simulia, 2014).

8.1 Mesh and boundary conditions

As mentioned earlier, various FE models are used to understand the HAGIS anchor performance. For example, 3D meshes are for the monotonic and cyclic performance of the skirt-plates system, and 2D axisymmetric FE meshes are used to develop equivalent spring models between plate and soil, estimate creep movement under sustained loading, and investigate the post-installation setup and setup stress (Figures 7-10).

The level of mesh refinement necessary to achieve convergence for simulations of skirts and skirt-plate systems was largely based on FE analyses of undrained loading of skirts in previous studies conducted by the research team (Al-Janabi and Aubeny, 2021). That study showed an element dimension at the soil-skirt interface, $a/D = 0.04$, could produce agreement between the FE and reference plastic limit analysis (PLA) predictions to within 4% (Al-Janabi and Aubeny 2022). Since this level of mesh refinement requires an unrealistically large computational effort, especially for the large number of load repetitions required for the cyclic load studies, a somewhat coarser mesh is adopted, $a/D = 0.08$. In this case the FE predicted load capacity exceeds the PLA reference solution by about 6-8%.

For simulations focusing on plate anchor behavior, the level of mesh refinement is established by comparing FE solutions to published solutions for single embedded circular disks given by Merifield et al. (2003), Merifield (2011), and Wang et al. (2013). Based on these comparisons, an

element dimension at the plate-soil boundary a/D=0.05 is adopted for the studies presented herein. This element size produces FE solutions that match the reference solutions to within 1.5%.

8.1.1 Monotonic simulations on plates and plate groups

The FE soil model uses a linearly elastic-perfectly plastic behavior beneath a Tresca yield surface and an associated flow rule. To approximate the undrained loading, the current study assumes a Poisson's ratio, with μ set to 0.49. Since the focus of the study can be separated as developing equivalent springs and characterization of interference effects on the plate group, FE studies took different undrained shear strengths varying from uniform (s_u=1kPa) for the interference effects to linear strength ($s_u=2+1.6z$ *kPa*) for developing equivalent springs. Additionally, all FE studies took Young's modulus E/su=150 or E/s_u=500, which does not affect the ultimate load capacity of the anchor (Chen 1975).

Firstly, a two-dimensional axisymmetric was used to investigate the force-displacement relationship of a single helical plate (Figure 7). The soil was modeled using first-order, fully integrated elements (4-node bilinear elements, CAX4), with the boundary placed 10 equivalent diameters away from the plate. The plate was assumed as a rigid body. Element dimensions varied from about 1/40 of the plate circumference near the plate-soil interface to 0.1 m in regions far from the plate.

Secondly, the soil domain for the plate grouping effects was modeled using first-order and fully integrated hybrid elements (eight-node element, C3D8H). The boundary was positioned from two to five diameters of the plate away from the helical plate to simulate the constraint conditions on the central plate, caused by adjacent plates from the plate group (Figure 8.a.). Element dimensions varied from about 1/50 of the plate circumference near the plate-soil interface to 0.1 m in regions

far from the plate. Parallel cyclic symmetry 3-D FE mesh also was carried out to evaluate the symmetric shaped plate array (Figure 8.b.). By using the Quadratic tetrahedron element type (C3D10) with sufficient boundary distances for the numerical model equal to 4m horizontally, and 30m vertically. The cyclically symmetric configuration comprised 8 plates embedded at a depth of 20m. The analyses were conducted for four cases of anchor spacing: 2.5*B,* 3*B,* 4*B,* and 5*B*, where *B* is the plate diameter.

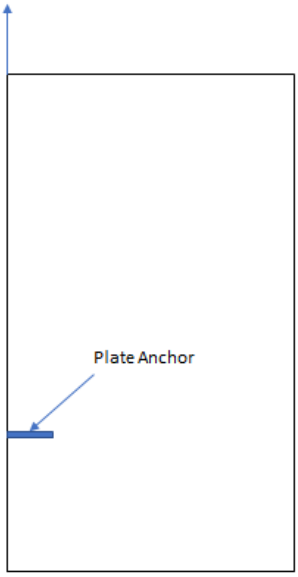

Figure 7: An axisymmetric FE model for developing equivalent springs, estimating creep and consolidation effects.

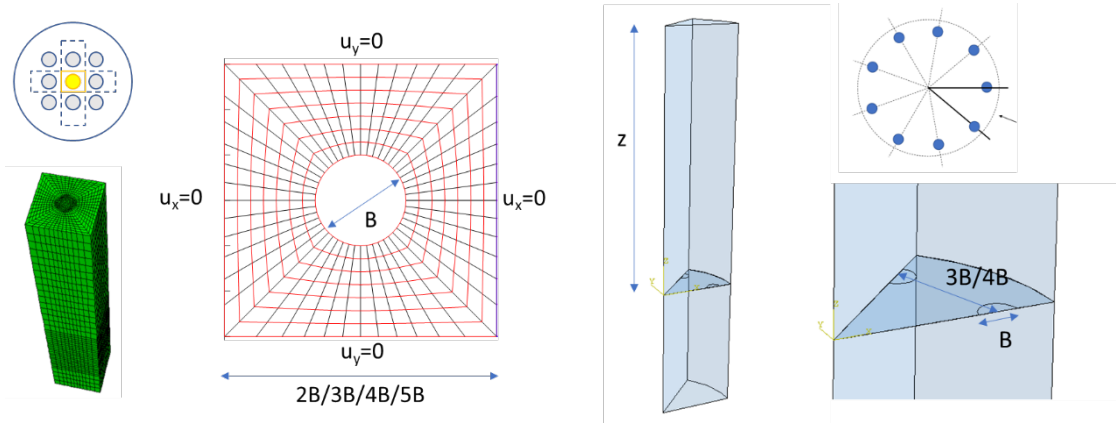

a) 3-D FE mesh b) Cyclic symmetry 3-D FE mesh

Figure 8: 3-D FE mesh for interference effect.

8.1.2 Monotonic and cyclic simulations on skirt and skirt-plate system

A nonlinear kinematic hardening model was used to simulate the monotonic and cyclic responses of caissons/ HAGIS. This model is available in commercial FE (Simulia, 2014), and it is an extension of a basic model comprising a von Mises failure criterion with an associated flow rule.

A three-dimensional mesh comprised of 8-node, bilinear brick elements, with full integration, models the soil domain. The mesh is cylindrical mesh with a lateral far-field boundary located 7D from the centerline (Figure 9). The depth of the mesh is fixed at about 6L. The bottom boundary is restrained in all directions. An 8-noded linear brick, fully integrated, hourglass control (C3D8) was used to model the soil. The level of mesh refinement provides reasonable match to reference solutions with acceptable computational times. Nodes at the soil-caisson interface were tied together. To model less than full adhesion, $\alpha < 1$, the nodes at the interface were still tied together, but the soil strength in the elements at the soil-caisson boundary was reduced by a factor α.

The skirt was simulated as a rigid shell. The FE model imposes no failure mechanism but, for vertical loading, all results showed reverse end bearing failure of the interior soil plug to be the

critical mechanism. This mechanism is in contrast to pullout of the skirt itself, with no soil attached to it.

For the monotonic simulations, the plates and cables were modeled as nonlinear spring behavior by specifying a force–relative displacement between two selected nodes, one on the skirt plate and one at the plate anchor depth. These springs were connected to the skirt to simulate the HAGIS as shown in Figure 9. The force-relative displacement values were found from an axisymmetric analysis.

For the cyclic simulations, the nonlinear spring elements were unable to capture the cumulative displacement. Therefore, the plates were modeled as a rigid body (bind a set of nodes) and connected to the skirt by spring elements to simulate the cables as shown in Figure 10.a-b.

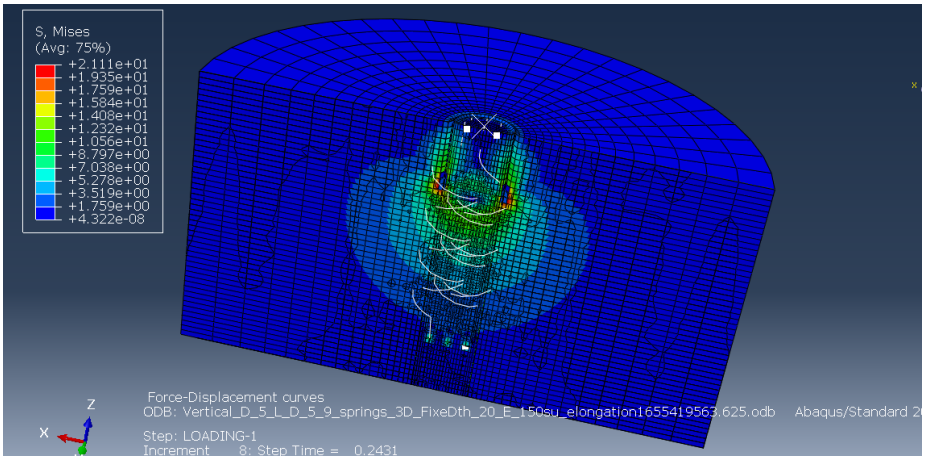

Figure 9: Monotonic simulation setup.

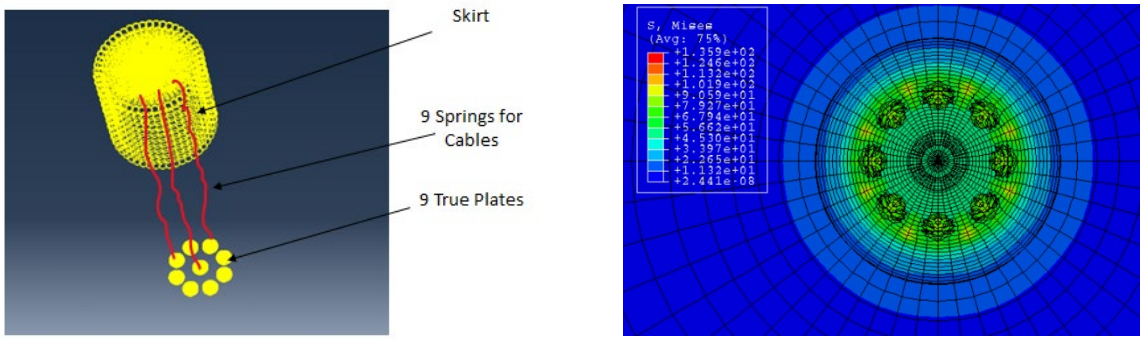

a) Skirt, springs, and plates b) Plates as rigid bodies

Figure 10: Cyclic simulation setup.

8.1.3 Creep simulations

An axisymmetric FE model was modeled using ABAQUS 6.14 for the creep test of a single plate (Figure 7). The modeling space chosen for the soil was a 2D axisymmetric continuum. A 4-node bilinear element, fully integrated, hourglass control (CAX4) was used to model the soil. The plate was modeled as a rigid body.

9. Parametric Study

9.1 Monotonic simulations of plate

In order to understand the force-displacement relationship between plate and soil, the current study estimated the following parameters: adhesion factor between plate and soil, and remolded zone above the plate (see Table 6). The assumed soil profile for developing equivalent springs is a typical normally consolidated clay (undrained shear strength $s_u=2+1.6z$). Since the focus of this study is the characterization of the anchor performance of the skirt-plate system, all FE studies took a uniform plate size (d_p=0.4m) and the same embedment depth (z=20m). Figures 12 and 13 shows the force-displacement relationship between soil and plate. Figure 12 shows the adhesion

factor to have a minor effect on the uplift resistance of the plate. Reducing the soil-plate adhesion factor from 1.0 to 0.4 is predicted to reduce the anchor plate tensile load capacity by about 6.6%. A possible explanation for this trend is that a relatively small portion of the collapse mechanism for a loaded plate involves slippage at the soil-plate interface; namely, slippage of soil at the edges of the plate. Elsewhere, the collapse mechanism comprises soil flowing from top to bottom around the plate, as the plate uplifts. Internal shearing of the soil in this flow-around collapse mechanism is largely unaffected by conditions at the soil-plate interface, so the influence of the adhesion factor is relatively minor.

By contrast, a remolded zone of soil above the plate significantly impacts the axial resistance of the plate. Figure 13 shows the effect of soil remolding in a column of soil extending above the plate to the ground surface. The predictions are expressed in terms of the inverse of sensitivity ($1/St=S_r/S_i$), where S_r/S_i varies from 0.4 to 1.0. Up to 20.9% reduction in tensile load capacity occurs over the range of soil strength reduction considered in the parametric study. The load-displacement relationships shown in Figures 12 and 13 were used to develop equivalent spring elements for plate resistance in subsequent monotonic studies of skirt-plate system behavior. It is noteworthy that the reduction in plate anchor uplift load resistance due to soil remolding is not directly proportional to the reduction in soil strength in the column of soil above the plate anchor. The reason for this is that the pullout failure mechanism mobilizes soil resistance in both the remolded column of soil and in the intact soil outside of the zone of remolding.

Table 6: Parametric study for developing equivalent springs.

Conditions	Considerations	Parameters
Plate diameter: 0.4m, Embedment depth: 20m	Wished-in-place: Adhesion factor (α) between plate and soil	α=0.4, 0.6, ,0.8, and 1.0
	Remolded zone above the plate (Post-installation 38tress)	Remolded stress/Initial stress =S_r/S_i=0.4, 0.6, 0.8, and 1.0

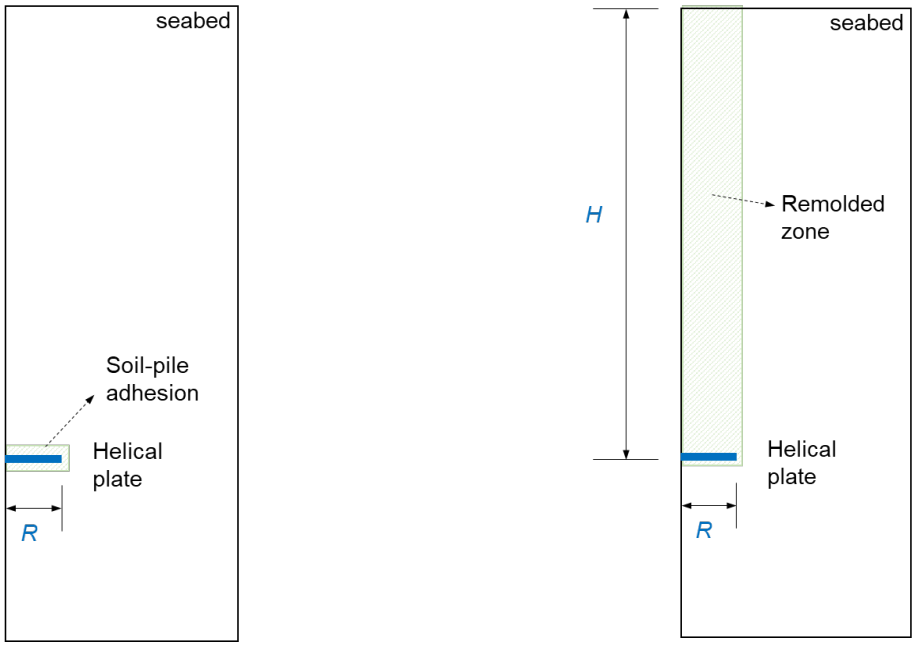

a) adhesion effect b) Soil remolded zone effect

Figure 11: Developing equivalent springs for plate resistance.

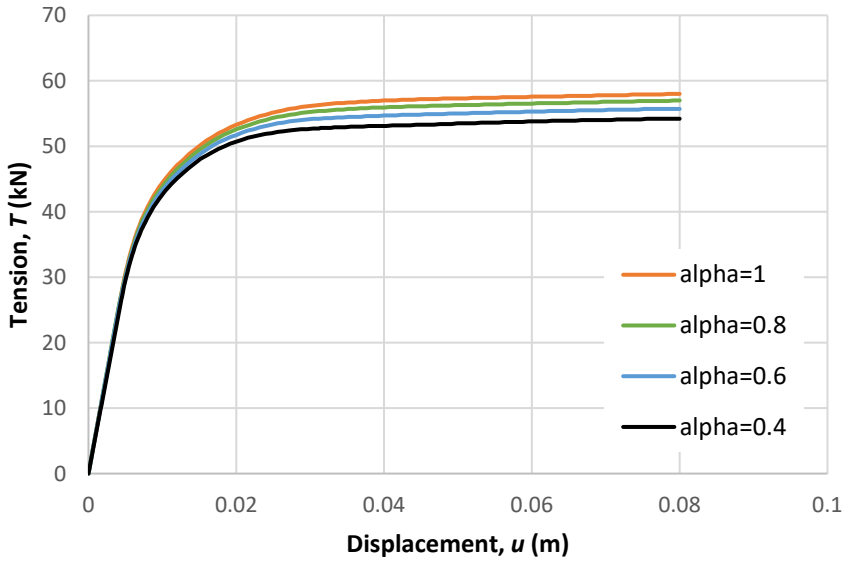

a) Tension force vs. displacement

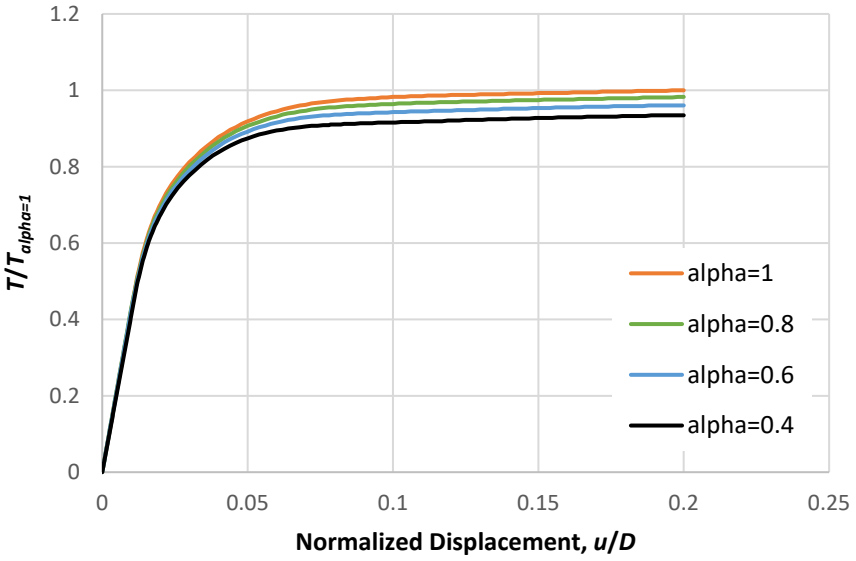

b) Normalized tension force vs. normalized displacement

Figure 12: Equivalent spring input for plate resistance (adhesion effect).

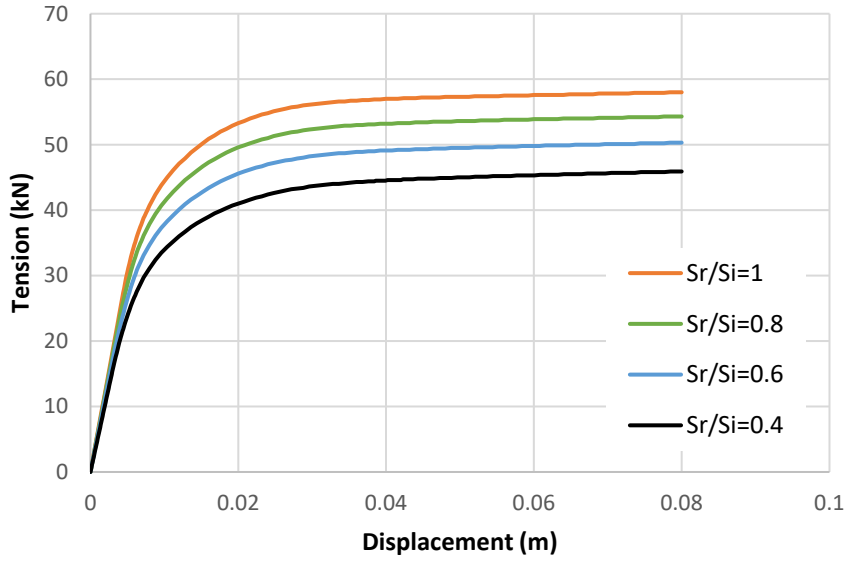

a) Tension force vs. displacement

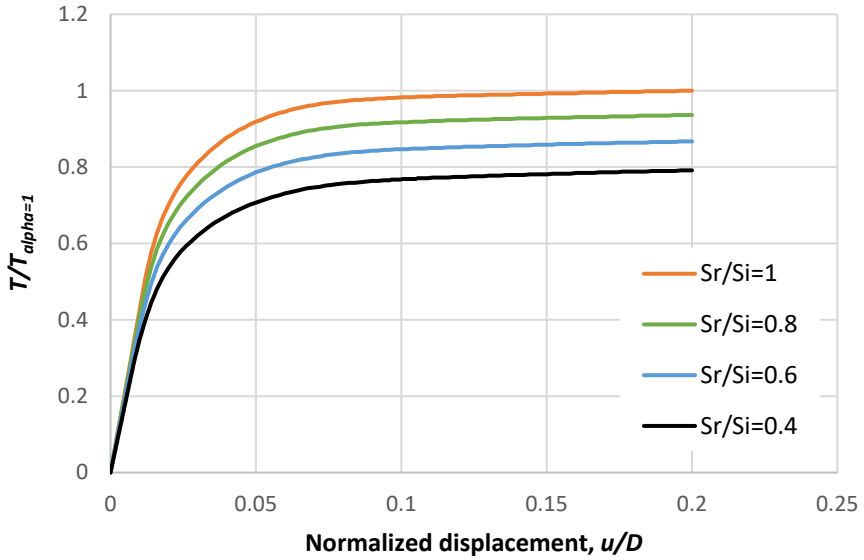

b) Normalized tension force vs. normalized displacement

Figure 13: Equivalent spring input for plate resistance (Remolded zone effect).

9.2 Monotonic simulations of plate groups

This study evaluated the spacing distance between helical plates to understand how it alters the failure mechanism and ultimate capacity of the plate groups. Since the HAGIS plate configurations vary, this study considered two configuration cases. The first study (Figures 8.a. & 15.a.) analyzed the performance of the plate in a square (equal spacing in both directions) three-by-three array of plate anchors. The second study analyzed the performance of plates arranged in the circular array shown in Figures 8.b. & 15.b. For the former case, a single plate was analyzed, with zero horizontal displacement was imposed at the far-field boundaries to impose a symmetry condition between the central plate and the adjacent plates. For the latter case, horizontal displacement was imposed at the wedge boundaries to impose a cyclic symmetry condition.

As mentioned above, the soil assumed as uniform and undrained loading conditions (Poisson's ratio=0.49) are assumed in the analyses. Figure 14.a. shows the relationship between maximum load capacity of a single plate versus center-to-center spacing of the plates. Computed load capacity is normalized the by load capacity of a plate that is essentially unaffected by interference effects, which the analyses indicate to be at a spacing greater than 3*B* (where *B* is plate diameter) for the case of the 3x3 rectangular spacing grid. At the lowest spacing analyzed, a center-to-center spacing of 2*B*, the interference effect results in about a 12% reduction in uplift capacity.

In the case of plate anchors arranged in a circular pattern at a 2-m radial distance from the skirt centerline, the number of plates *N* analyzed in the parametric study varied from 6 to 15 (Figure 14.b.) corresponding to a range of angular spacing ranging from 60 to 24 degrees, or plate spacings varying from 5 to 2.1 *B*. The FE analyses show that for spacings greater than about 3.8*B* the interference effect is negligible. For spacings less than 3.8*B*, the capacity reduction is noticeable, but less than 5%. The predicted capacity for a spacing of 5*B* is actually somewhat less than that

for 3.8*B*. This apparent anomaly is likely a consequence of the modest differences in the FE meshes, and is not considered to be of physical significance.

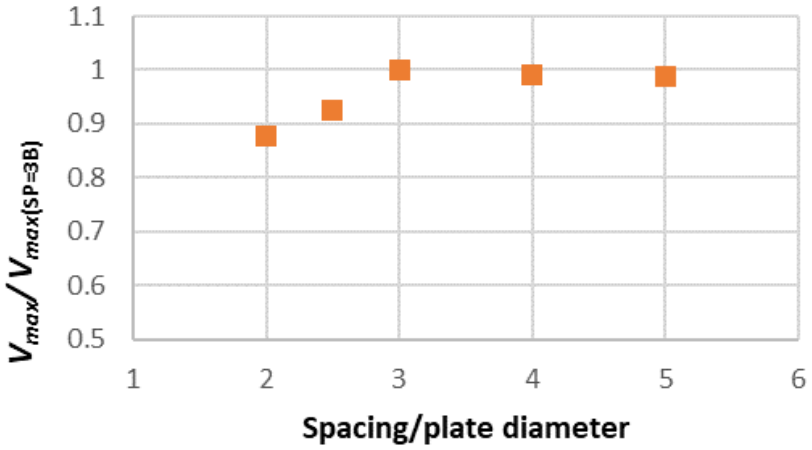

a. Predicted interference effect for center plate in 3x3 rectangular plate anchor grid

N	Phi	Spacing/Plate Diameter	V/Vmax
6	60	5.0	0.97
8	45	3.8	1.00
10	36	3.1	0.98
12	30	2.6	0.95
15	24	2.1	0.96

b. Cases considered in parametric study for circular plate pattern

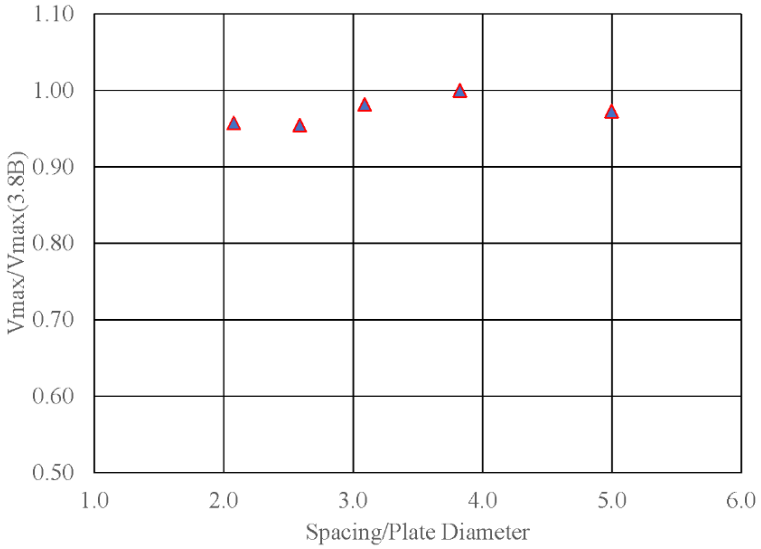

c. Predicted interference effect for plates in circular pattern

Figure 14: Effect of plate anchor spacing on load capacity.

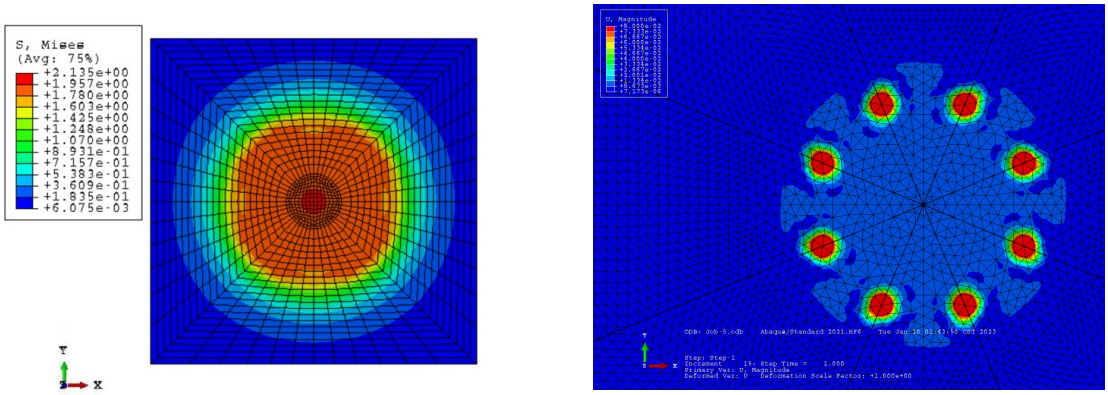

a) 3 by 3 matrix configuration (center plate) b) Circular configuration

Figure 15: Stress contour of the plate groups.

9.3 Monotonic simulations of skirt-plate system (HAGIS)

A series of monotonic simulations were conducted to evaluate the ultimate load for different HAGIS setup configurations (see Table 3). Figure 16.a-c. shows the anchor plate (modeled as springs) patterns for the following systems: a 5-m diameter (D) skirt with 9 deeply embedded plate anchors, an 8-m diameter skirt with 30 deeply embedded plate anchors, and a 10-m diameter skirt with 55 deeply embedded plate anchors plate anchors. Each of these cases was modeled for skirt aspect ratios L/D = 0.5 and 1, where L = skirt length.

Figure 17 shows a comparison between the ultimate load capacity under purely vertical loading for the HAGIS system for a skirt diameter of 5 m. First considering skirts alone, with no plate anchors, doubling the skirt depth more than doubles the vertical load capacity. This is a consequence of the combined effects of a longer skirt (more surface area) and the linearly increasing undrained shear strength with depth. It is noted that, in a soil profile where soil strength increases linearly with depth, the pile capacity increases parabolically with depth, since surface area of the pile also increases linearly with increasing depth. The addition of helical plates to the skirt increases the vertical load capacity by about 150% for the L/D = 0.5 case and by about 60% for the L/D = 1 case. This behavior simply reflects the fact a shallower skirt has less vertical load capacity; therefore, when plates are added to a shallow skirt the relative increase in vertical load capacity is greater. This should not be construed to imply that the helical plates are somehow less effective for longer skirts – the contribution of the plate anchors to overall vertical load capacity is actually quite similar for the shallow and long skirts systems. The numerical simulations show similar trends in behavior can be seen for the skirt diameters evaluated in this study, 8 m and 10 m, as shown in Figures 18 and 19.

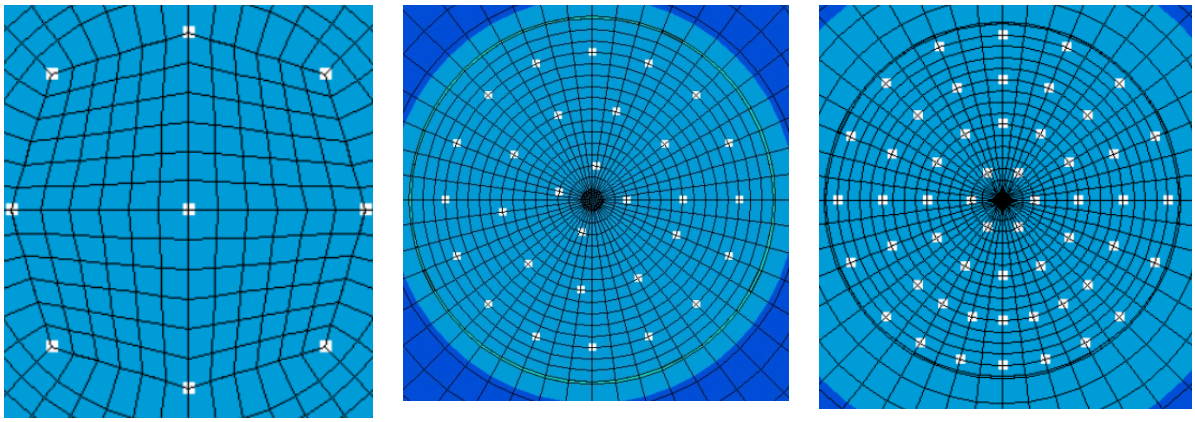

a) 9 Springs, Spacing ~3B. b) 30 Springs, Spacing ~3B. c) 55 Springs, Spacing ~3B.

Figure 16: Anchor plate patterns.

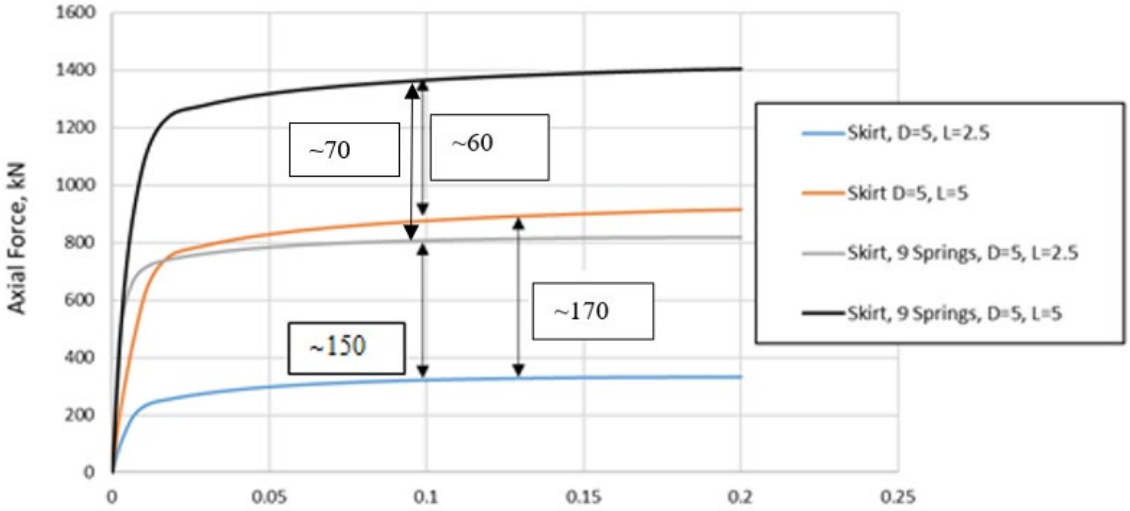

Figure 17: Vertical force vs displacement for skirt only and skirt + 9 plates.

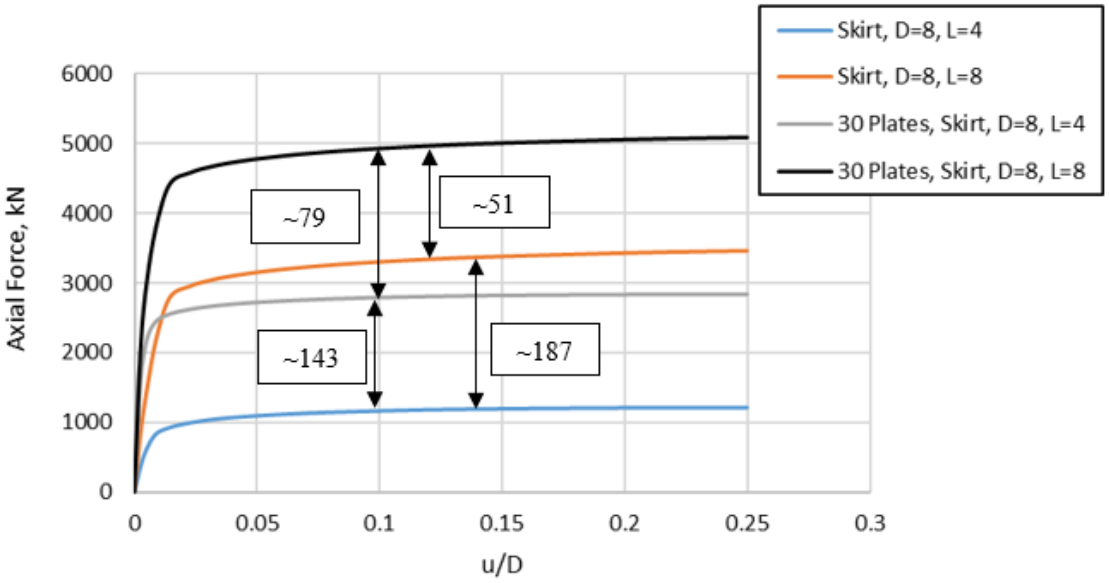

Figure 18:Vertical force vs displacement for skirt only and skirt + 30 plates.

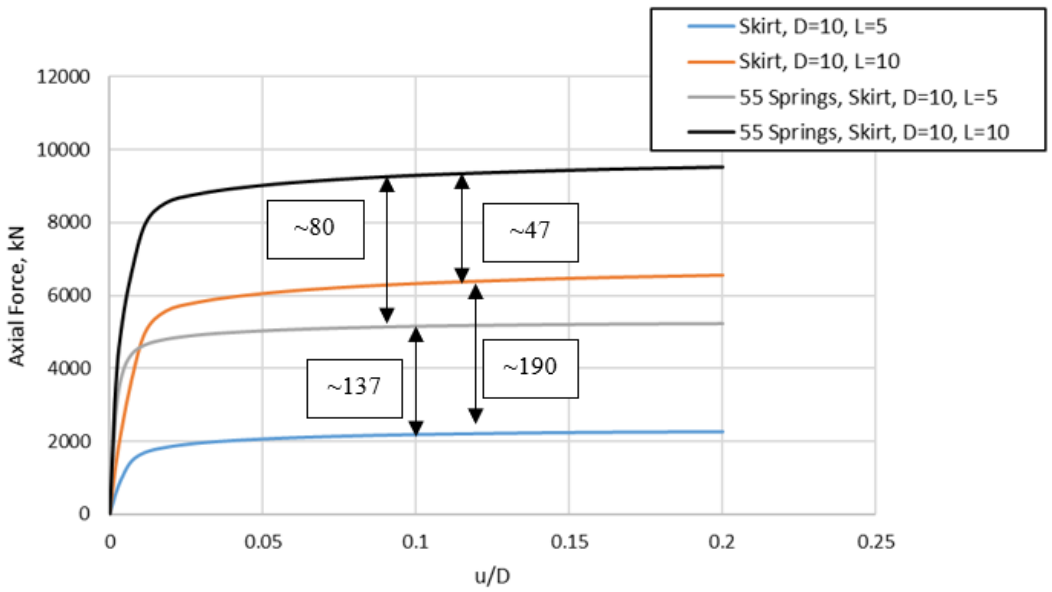

Figure 19: Vertical force vs displacement for skirt only and skirt + 55 plates.

Figures 20-22 show the predicted performance of the HAGIS system under purely horizontal loading. This study considered aspect ratios L/D = 0.5 and 1, and skirt diameters of 5 and10 m. The increase in the ultimate capacity due to the anchor plates is in the order of 10%-30%. The modest increase in horizontal load capacity due to the anchor plates is expected, since the contribution to load capacity from the anchor plates is primarily in the form of axial load capacity. Since the plate anchor cables are initially vertical, the contribution to horizontal load capacity is expected to be small. The fact that the anchor plates contribute at all to horizontal load capacity can essentially be attributed to the geometric nonlinearity of the loaded system. As the skirt translates horizontally under loading, the anchor cables are no longer purely vertical, so the anchors can then resist a small component of the horizontal loading.

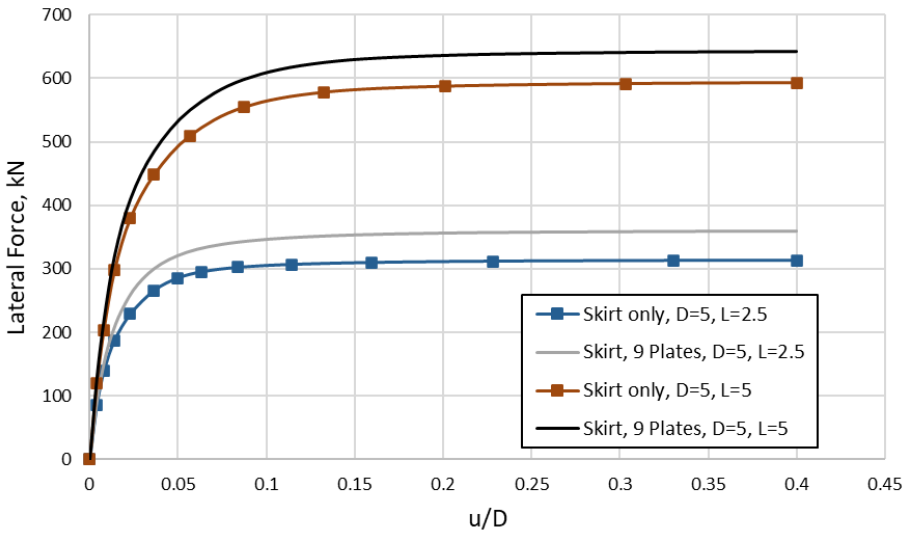

Figure 20: Horizontal force vs displacement for skirt only and skirt + 9 plates.

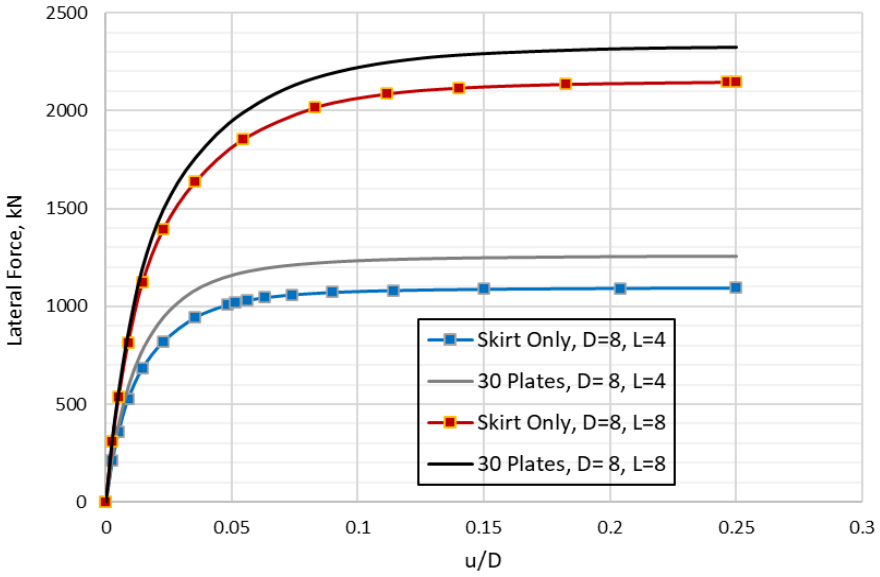

Figure 21: Horizontal force vs displacement for skirt only and skirt + 30 plates.

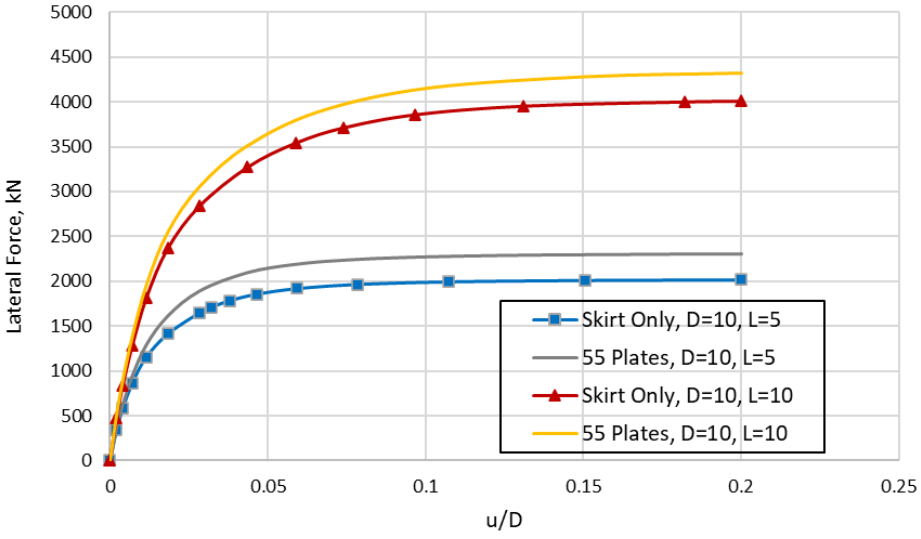

Figure 22: Horizontal force vs displacement for skirt only and skirt + 55 plates.

Figures 23-25 show the predicted performance HAGIS system under inclined loading, with a 45-degree applied load angle. The study compares aspect ratios L/D = 0.5 and 1 for skirt diameters of 5 and10 m. As noted earlier for the case of no plate anchors, the load capacity of the longer skirt is more than double that of the shallower skirt. Addition of plate anchors to the system increases the ultimate capacity by about 50%-140% for the long and shallow skirts respectively. It is noteworthy that the effectiveness of the anchor plates under inclined loading is somewhat less than that under purely vertical loading. This is a likely consequence of the fact that, under purely vertical loading, all plate anchors mobilize their full resistance to uplift. By contrast, under inclined loading, the rotation of the skirt prevents full mobilization of uplift resistance in some of the plates. For example, rotation of the skirt in response to the horizontal component of loading will cause the plate anchors on the windward side of the skirt to displace upward a greater distance than those on the leeward. Thus, the contribution to load capacity from the leeward plate anchors is expected to be smaller than that from the windward plates.

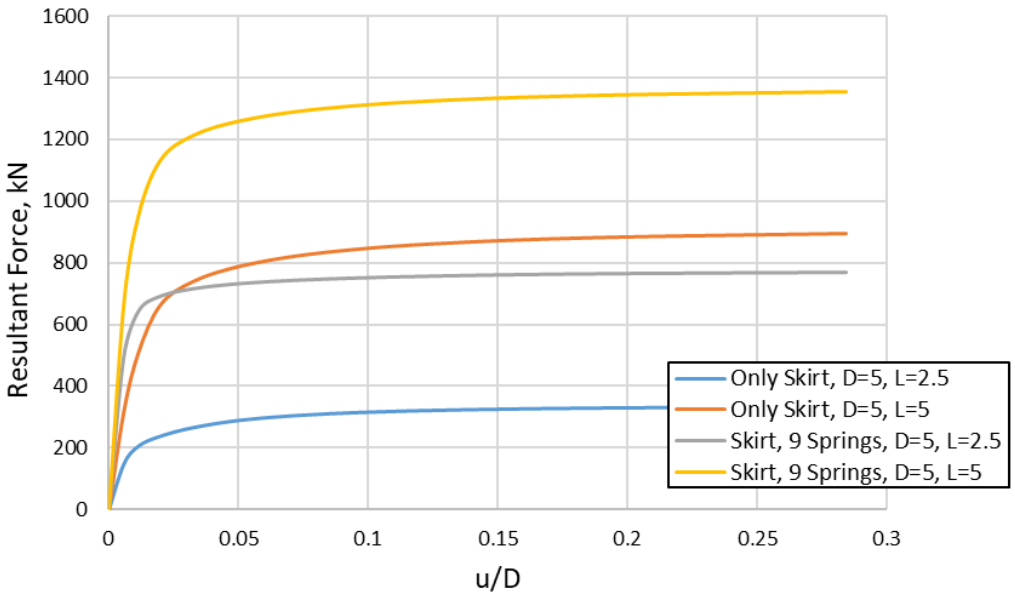

Figure 23: Inclined 45° loading, force vs displacement for skirt only and skirt + 9 plates.

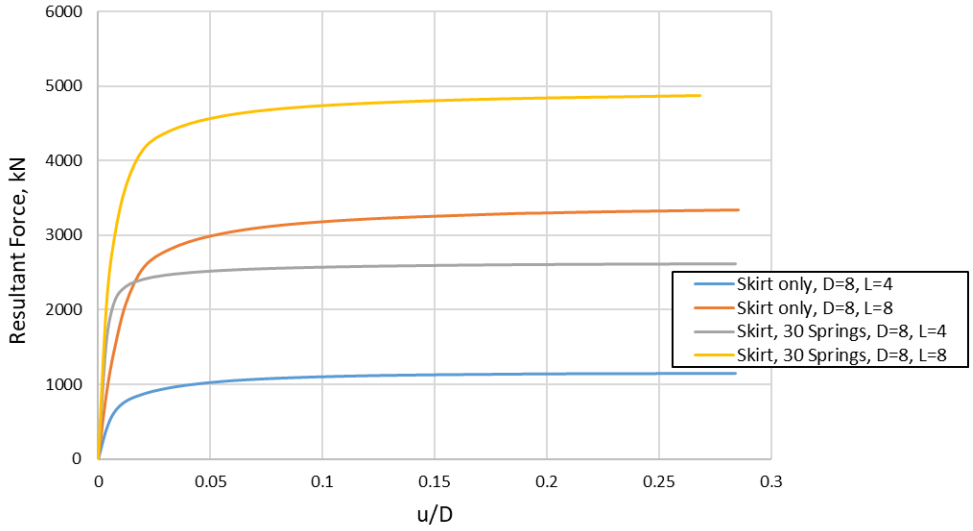

Figure 24: Inclined 45° loading, force vs displacement for skirt only and skirt + 30 plates.

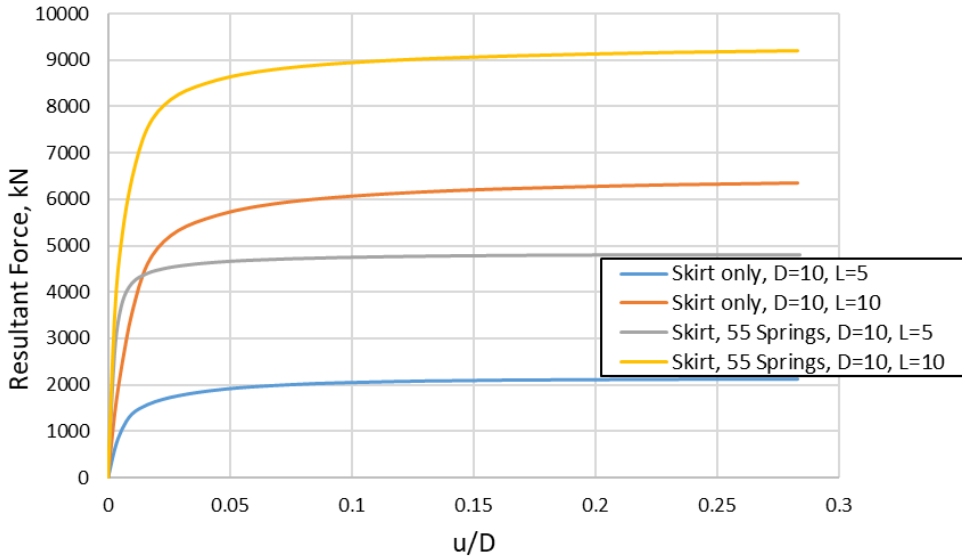

Figure 25: Inclined 45° loading, force vs displacement for skirt only and skirt + 55 plates.

9.4 Cyclic simulations

Using the calibrated FE model by Al-Janabi and Aubeny (2021), a parametric study was conducted to predict cumulative deformations during force-controlled cyclic loading. Storm loading on offshore anchors typically comprises a series of load cycles having non-uniform load amplitudes. However, the analysis of cyclic loading is often conducted in terms of equivalent uniform load cycles, or series of packets of load cycles with uniform load magnitudes within a packet. The cyclic loading analyses performed in this study were, unless otherwise stated, for repeated loads at one-half the allowable load level, or one-quarter of the load capacity of the anchor. This reflects the fact that usually only a single load cycle occurs at the allowable load level, with repeated load cycles occurring at load levels well below the peak load. The number of load cycles that occur at this load level (i.e. one-half the maximum allowable load) depends on site specific storm loading conditions. Based on a typical storm loading history presented by Andersen (2015), this study performs numerical simulations for 50-100 load cycles at one-half the allowable load level. Noting that load levels are well below the ultimate value, the primary focus of the cyclic loading studies is the cumulative permanent displacement that occurs under repeated load cycles. All simulations in this study involved uniform load amplitudes with zero load reversal. In this study, 5-m diameter skirt with aspect ratio of L/D = 0.5 was examined for a load inclination range $\psi = 0^{\circ}$- 90°.

A clay profile for a normally consolidated clay was used, with a shear strength of 2 kPa at the mudline and increasing with depth at a rate of 1.6 kPa/m. A strength reduction equal to the adhesion factor ($\alpha = 0.8$) was assigned to the elements adjacent to the pile to model the interface effect. This value was selected based on field studies by Jeanjean (2006) showing post-setup values of α lying in a range 0.65-0.90 for suction caissons in normally consolidated clays. The initial yield stress was set to 0.1 of the maximum stress (Al-Janabi and Aubeny, 2021; Anastasopoulos

et al. 2011). All simulations were for a soil elastic modulus E/s_u of 150. All the skirts were loaded at the top of the skirt at its centerline.

In this study, the ultimate load capacity (F_{ult}) of the system was estimated from monotonic loading simulations. A safety factor $FS = 2$ was applied to compute the maximum allowable operational load (F_{all}) for all cases analyzed. Figures 26 - 32 show the normalized cumulative displacements for different ψ of 0°-90°, E/s_u of 150, σ_0/σ_{max} of 0.1, and a soil-caisson interface adhesion factor of α of 0.8.

Figure 26 shows the predicted load-displacements loops during purely vertical cyclic loading for a HAGIS with 9 plates at 20 m embedment depth. Figure 27 shows the same simulation in terms of cumulative displacement versus load cycle. Displacements are normalized by the skirt diameter. The predictions show that permanent displacements accumulate under cyclic loading, to the extent that the cumulative displacement after 50 load cycles is nearly twice that occurring after the first load cycle. The rate at which permanent displacement accumulates decreases with increasing number of load cycles. However, after 50 load cycles the cumulative displacement is still increasing. It is not clear from this simulation as to whether the cumulative displacement will approach an asymptotic limit. However, since the anchor migrates upward into weaker soil has vertical displacements accumulate, there is no reason to expect that an asymptote exists. Figures 26 and 27 show that after 50 load repetitions (N=50) at one-half the allowable load produces cumulative displacements on the order of 0.3% for the purely vertical cyclic loading.

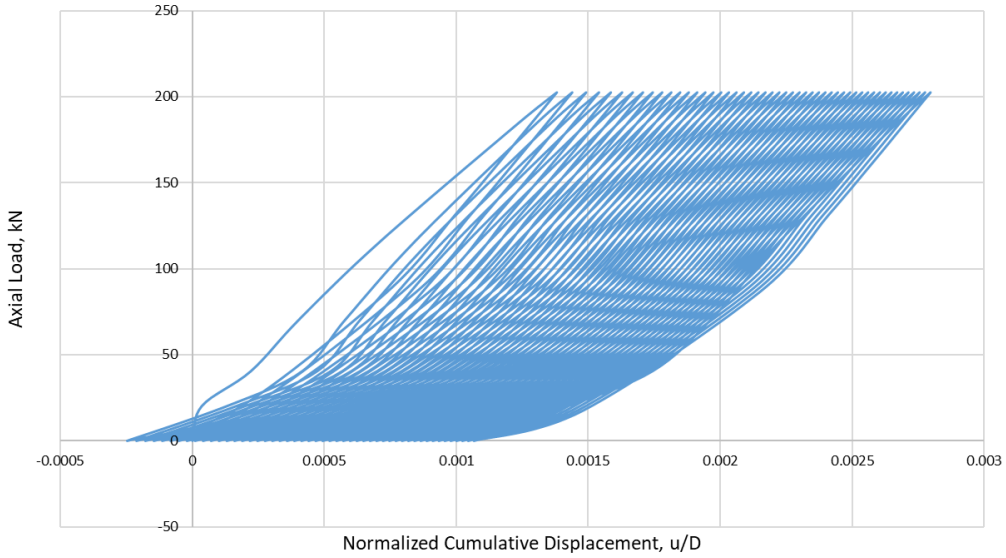

Figure 26: Load vs displacement during vertical loading of a skirt with 9 plate anchors.

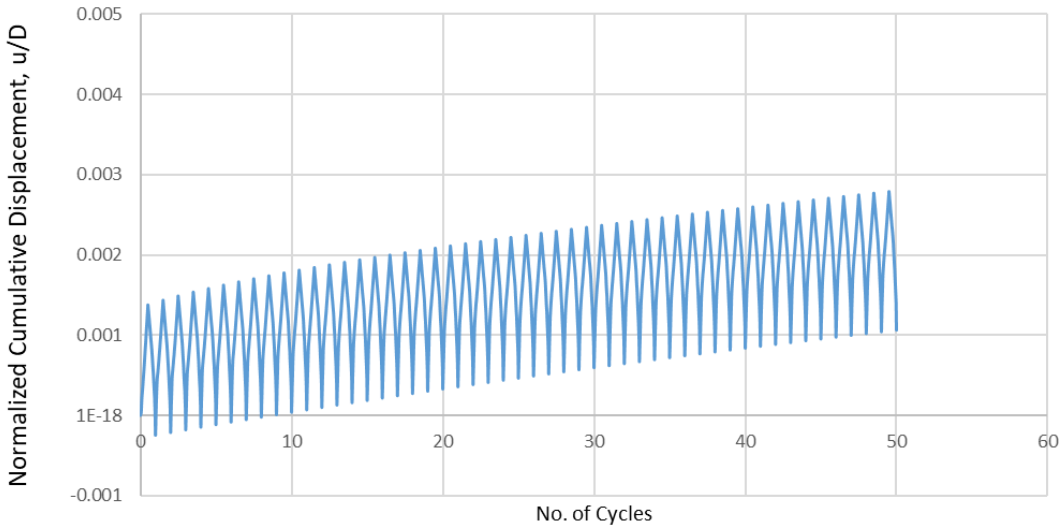

Figure 27: Displacement vs load cycle during vertical loading of a skirt with 9 plate anchors

.

Figure 28 shows load versus cumulative resultant displacement and Figure 29 shows resultant displacement versus load cycle for the case of inclined (45 degrees) cyclic loading. The resultant displacements were obtained by computing the magnitude of the combined horizontal and vertical components of displacement. In this case the load repetitions were taken to 100 cycles. Notably, the cumulative displacements under inclined loading are greater than under purely vertical loading. For example, after 50 load cycles the HAGIS displaced about 0.05 *D* under inclined loading, versus 0.003 *D* under purely vertical loading. Since the inclined cyclic load intensity was greater than the purely vertical cyclic load intensity, 260 kN vs 200 kN, the greater load intensity is one contributing factor to the larger displacements. Additionally, the load demand in the horizontal direction leaves less soil shearing resistance available to resist uplift. Figure 29 shows incremental displacements to be larger at the beginning of cyclic loading; however, the incremental displacements at larger numbers of load cycles do not tend to zero. This indicates that plastic deformations can occur indefinitely under sustained cyclic loading.

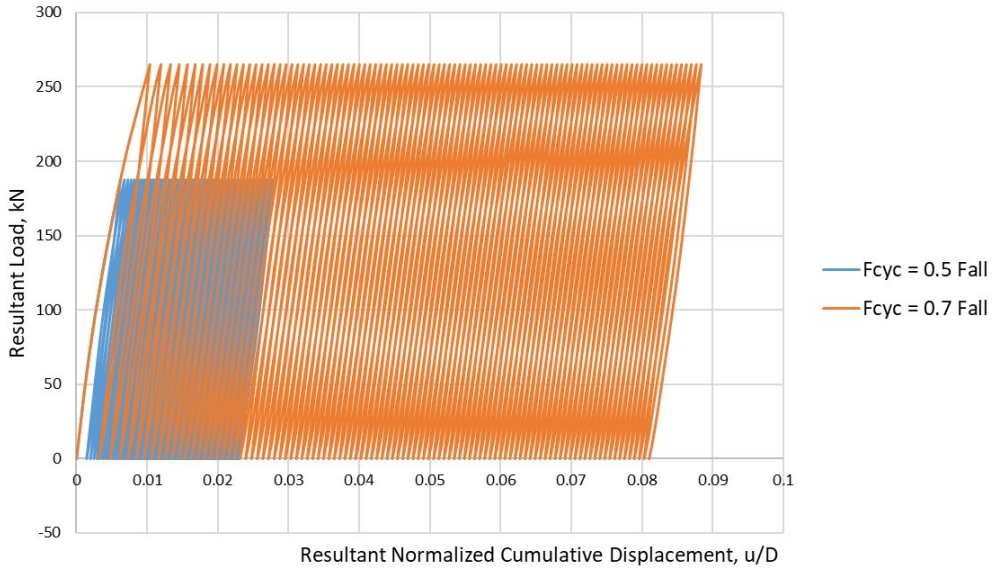

Figure 28: Load vs displacement during 45-degree loading of a skirt with 9 plate anchors.

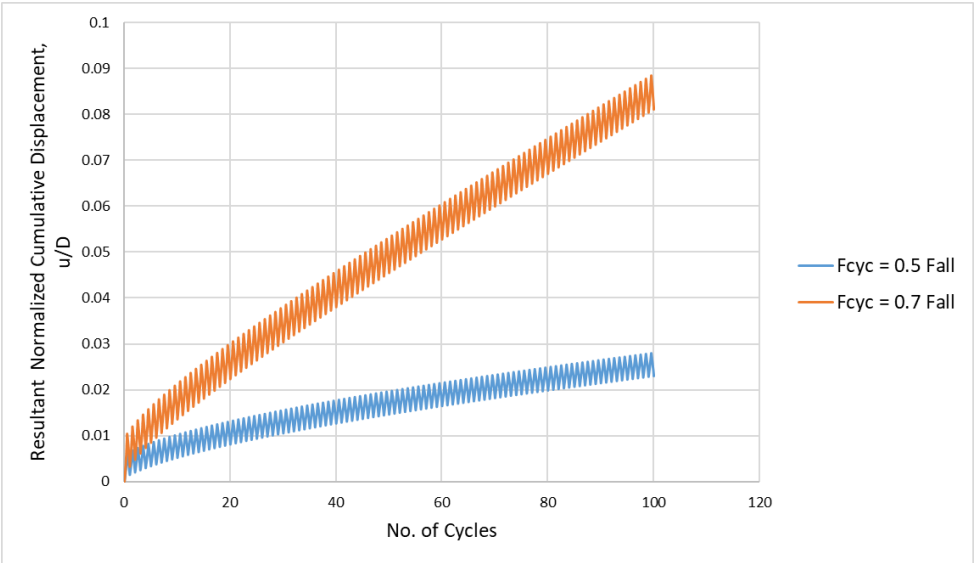

Figure 29: Displacement vs load cycle during 45-degree loading of a skirt with 9 plate anchors.

Figure 30 shows the separate vertical and horizontal components of displacement. The horizontal component is about 10 times the vertical component of displacement. That can be explained by

the rotation of skirt, where the skirt was loaded at the top of its centerline. This leads to rotating the skirt from the top (not purely skirt translation).

Figure 31 shows load resultant displacement versus load cycle for the case of purely vertical cyclic loading at large cyclic load levels relative to the analyses presented in Figures 26 - 29. In this series the cyclic load magnitude was set to F_{cyclic} = 0.5 F_{ult}, for the first 50 cycles of loading, to F_{cyclic} = 0.65 F_{ult}, for an additional 25 cycles of loading, and to F_{cyclic} = 0.8 F_{ult}, for the final 25 cycles of loading. This represents a rather severe loading sequence, since typical design practice usually assures only a single load cycle at 0.5 F_{ult} with cyclic load levels involving a large number (say 50 to 100) of repetitions being on the order of 0.25 F_{ult}. Nevertheless, Figure 31. shows generally tolerable displacements, so long as the cyclic load magnitude does not exceed 0.5 F_{ult}. Serious cumulative displacements do develop when this load level is exceeded; however, such loading would normally be considered to be unintended.

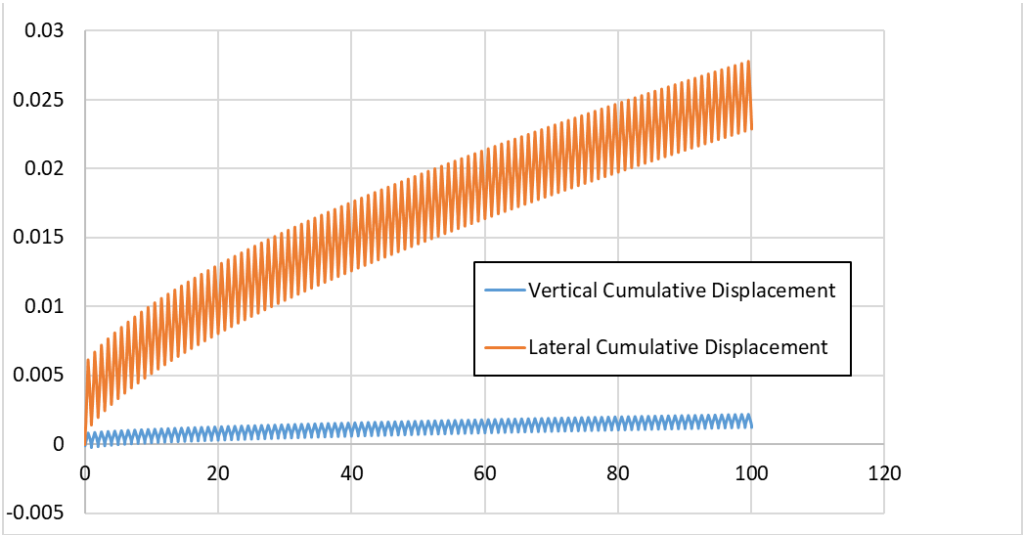

Figure 30: Displacement vs. load cycle (45 degrees) loading on skirt with 9 plates, (F_{cyclic} =F_{all}/2).

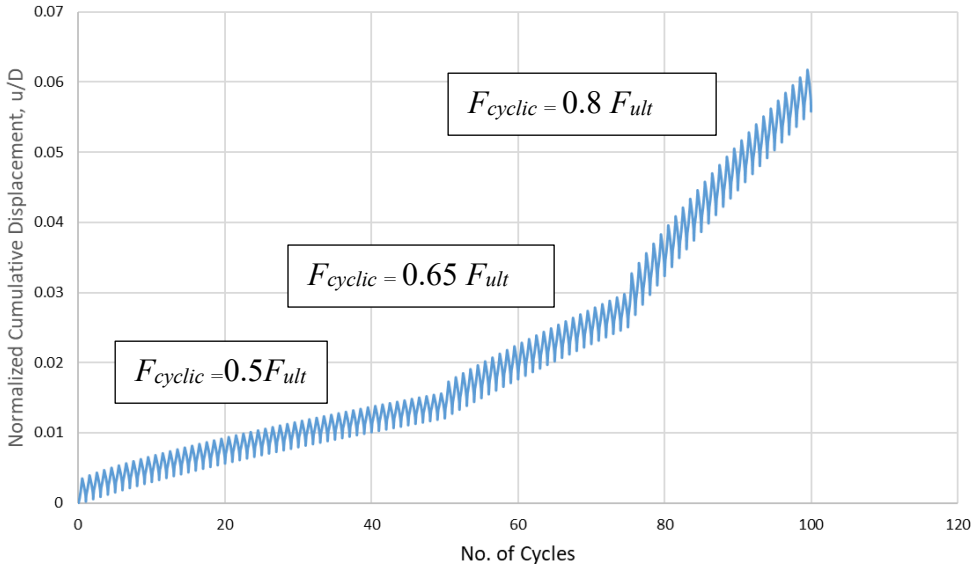

Figure 31: Vertical cyclic loading of skirt with 9 plates for different cyclic load levels.

Figure 32 shows cumulative displacement versus load cycle for the case of nearly vertical (10 degrees from vertical) cyclic loading. This figure shows the separate vertical and horizontal components of displacement. As in the previous series, this loading sequence is relatively severe, since normally an anchor is subjected to only a single cycle at a load intensity $F_{cyc} = F_{ult}/2$, with large numbers of repetitions occurring for load magnitudes well below this level. The predictions show vertical displacements to exceed the horizontal displacements.

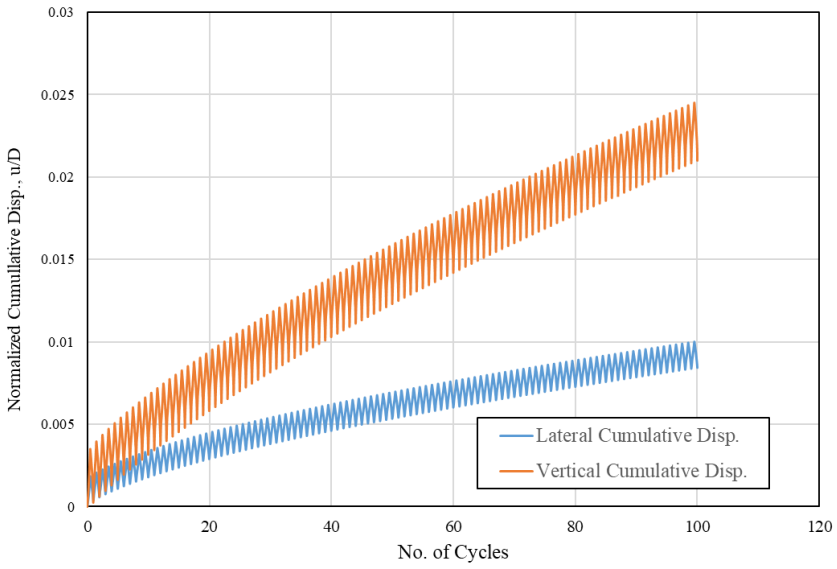

Figure 32: Displacement vs. load cycle for nearly vertical (10 degrees) loading on skirt with 9 plates, (F_{all} applied=F_{ult}/2).

General trends indicated by the cyclic loading studies include the following:

- There is little evidence that cumulative displacements approach an asymptote under sustained cyclic loading. However, this is not likely to be of serious consequence so long as the number of load cycles having a significant load intensity (e.g. F_{cyc} = 0.25 F_{ult}) does not exceed 50-100.
- Cumulative displacements under purely vertical loading are relatively minor, about 0.3% of the skirt diameter.
- Inclined loading, say 45 degrees from horizontal loading, appears to induce the most serious cumulative displacements. For similar cyclic load intensity levels, F_{cyc} = 0.25 F_{ult}, cumulative displacements for the inclined load case are about 10 times greater than those predicted for the case of purely vertical loading.

9.5 Creep simulations

The Prony series parameters were given by Swain and Ghosh (2019) for marine clay. A seven-parameter model used to describe the stress-strain behavior (Table 7). This study investigated creep effects for sustained loading, where the magnitude of the sustained load was a specified fraction of the allowable load F_{all}. The allowable load is taken as one-half of the ultimate load capacity of the anchor, i.e., the required safety factor of the anchor under vertical loading must be at least $F_{ult} / F_{all} = 2$.

Figures 33 - 36 show the strain vs. time relationship for different sustained load 25%-100% of the allowable load. The normalized displacement is about 1.2 for a sustained load at 50% of the allowable load. The reported strains are at the integration points of an element adjacent to the centerline directly above the plate, as illustrated in the figures.

An integration point (IP) is the point within an element at which integrals are evaluated numerically. These points are chosen in such a way that the results for a particular numerical integration scheme are the most accurate. The element type that we used for the creep tests is CAX4P which has 4 IPs.

Table 7: Prony series parameters.

Parameters	**g_1**	**t_1 (s)**	**g_2**	**t_2 (s)**	**g_3**	**t_3 (s)**
7	0.210	5.867	0.209	61.044	0.359	551.419

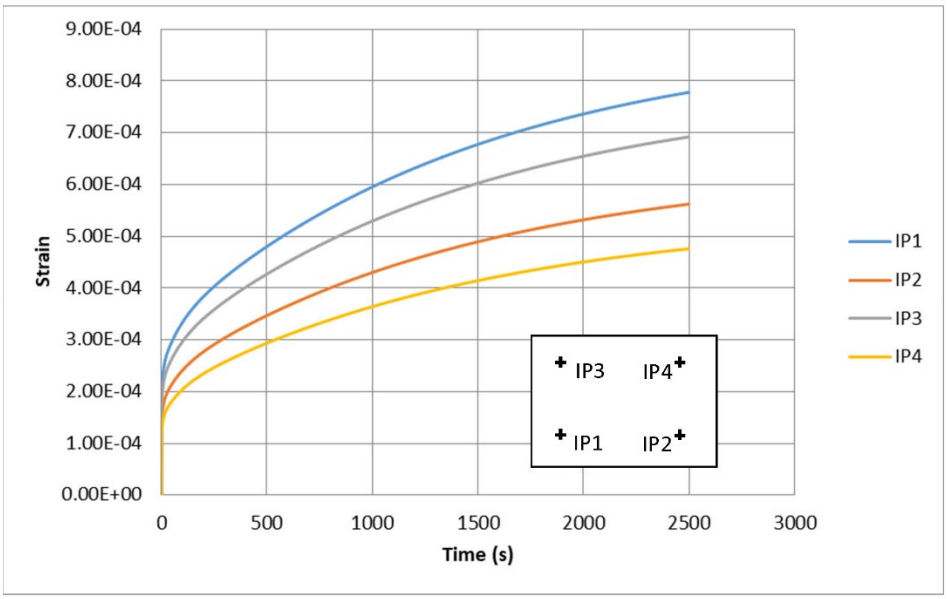

Figure 33: Integration strain vs. time curves for sustained load of 25% Fall.

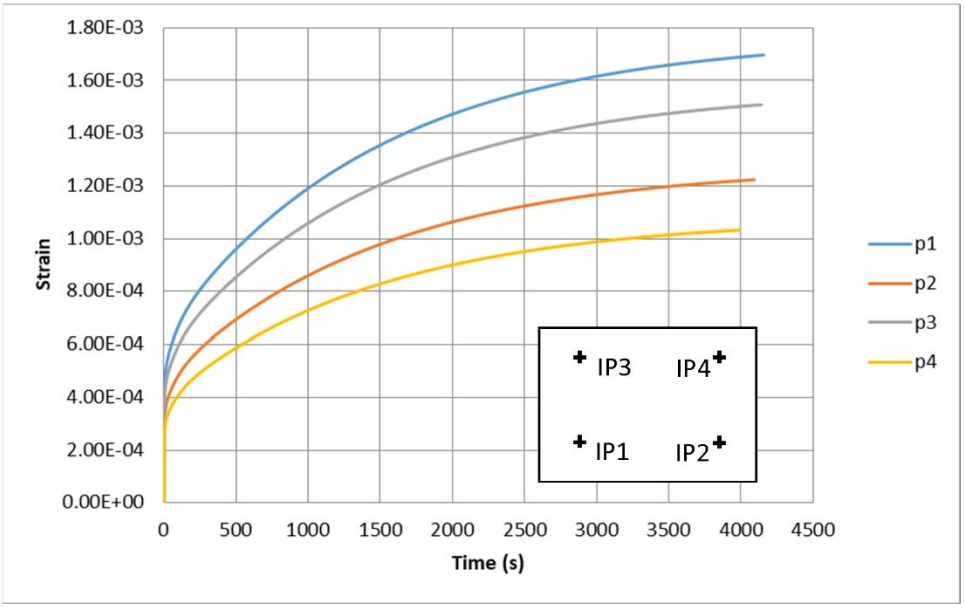

Figure 34: Integration point strain vs. time curves for sustained load of 50% Fall.

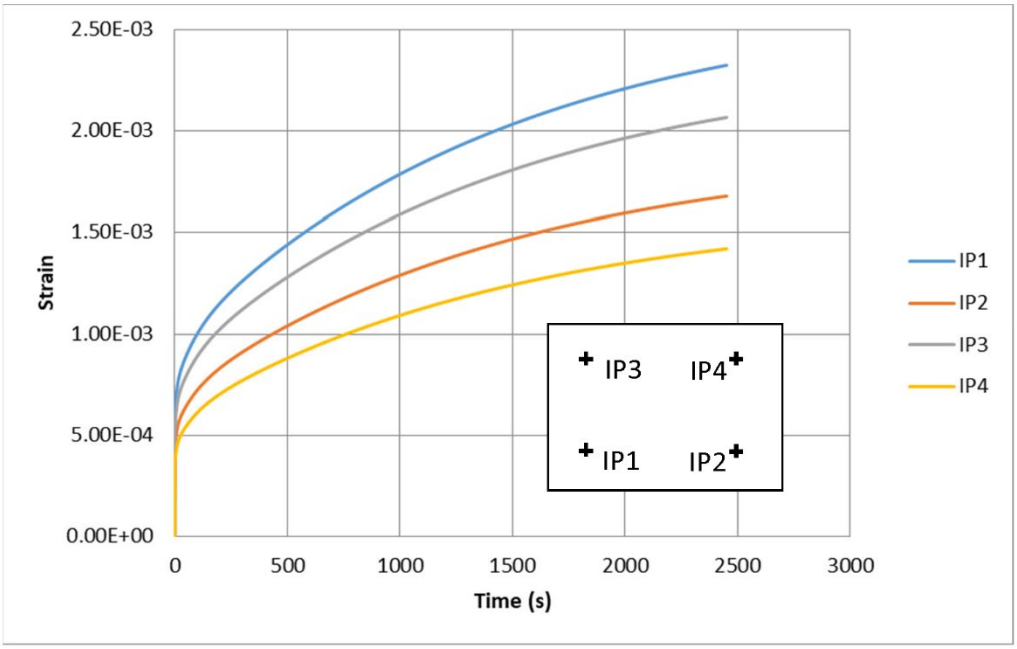

Figure 35: Integration point strain vs. time curves for sustained load of 75% Fall.

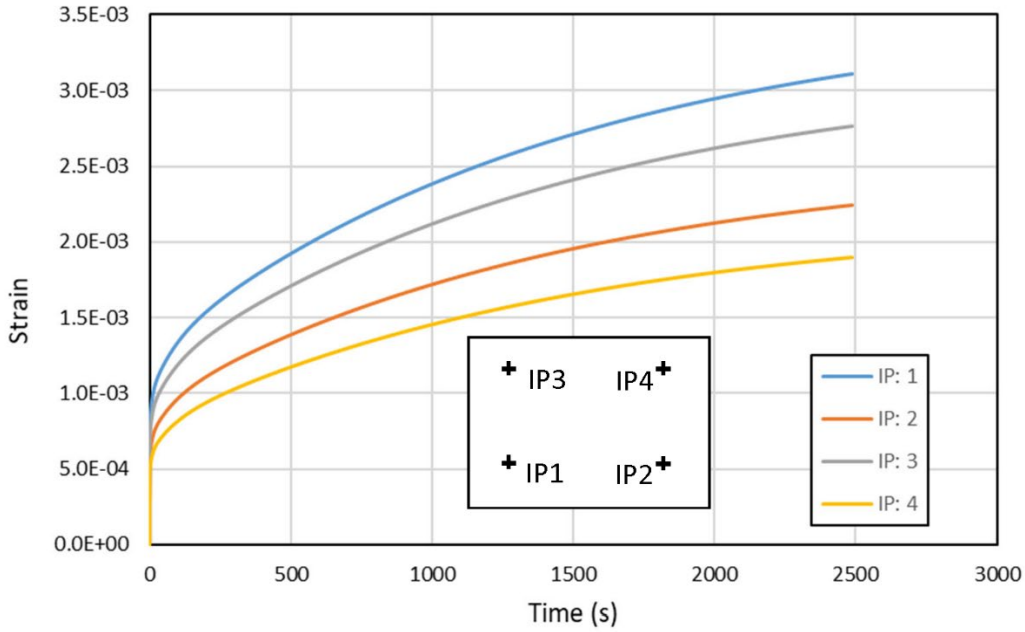

Figure 36: Integration point strain vs. time curves for sustained load of 100% Fall.

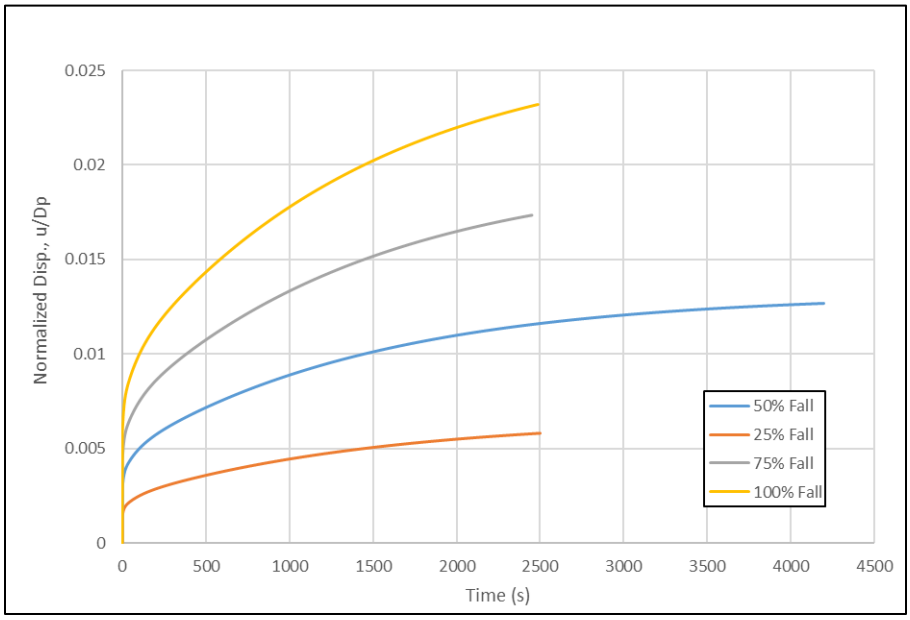

Figure 37: Normalized plate displacement (u/D_p = u/0.4 m) vs. time for different sustained loads.

9.6 Coupled-Consolidation Analysis

9.6.1 Consolidation Time Steps.

As mentioned earlier, due to the installation process of the helix, an excess pore water pressure is produced with an effect of reduced action in effective stresses through the soil zone above the helix which resulting remolded soil. Conventionally, consolidation processes in geotechnical engineering are expressed in terms of a dimensionless time factor T, defined as follows:

$$T = c_v t / R^2 \qquad \text{(Eq. 19)}$$

where c_v is the coefficient of consolidation, t = time, and R = a characteristic dimension, in this case, the plate radius. The coefficient of consolidation of consolidation c_v is defined by the following equation:

$$c_v = kM/\gamma_w \qquad \text{(Eq. 22)}$$

where k is soil permeability, M is the soil constrained modulus, and γ_w is unit weight of the pore fluid. Although the coefficient of consolidation is a commonly used soil parameter, it is not truly

a fundamental parameter; rather, it is the product of two fundamental parameters, *k* and *M*. Since elastic behavior in the MCC model is usually expressed in terms of bulk modulus *K* and shear modulus *G*, *M* can conveniently be expressed in terms of these parameters as follows:

$$M = K + 4G/3 \quad \text{(Eq. 203)}$$

In the MCC model the bulk modulus is not constant; rather, it is directly proportional to the mean effective stress *p*' (Eq. 24). The model parameter controlling the value of the bulk modulus is the parameter κ, which is related to the recompression index as defined by (Eq. 15).

$$K = \frac{(1 - e_o)\, p'}{\mathrm{k}} \quad \text{(Eq. 24)}$$

Different versions of the MCC model specify either shear modulus *G* or Poisson's ratio μ as being independent of stress level. This study adopts the latter approach, in which the shear modulus is proportional to bulk modulus according to the following equation:

$$G = \frac{K}{2}\frac{3\,(1 - 2\mu)}{(1 + \mu)} \quad \text{(Eq. 215)}$$

Since the bulk and shear moduli depend on mean effective stress, which varies throughout the consolidation process; thus, the coefficient of consolidation (62) is similarly stress level dependent. A question then arises as to what value of *p*' should be used when computing c_v. This study takes a *p*' value representative of the initial stress state of the soil, expressed as follows:

$$p' = \frac{\gamma' H(1 + 2K_0)}{3} \quad \text{(Eq. 226)}$$

where γ' is the soil buoyant unit weight, *H* is plate anchor embedment depth, and K_0 is the coefficient of earth pressure at rest.

Two main parametric conditions have been investigated in this study, which are the effect of the soil permeability coefficient *k*, and the effect of the helix embedded depth *H*. Table 8 shows the parametric study cases, that have values related to the expected condition range for this study. Therefore, the study focused on investigating the permeability changes when the helix embedded depth at 20m. Further, it has been examined the effect of the helix embedded depth with a range (5m, 10m, 20m) when the permeability coefficient is equal to 5e-7 m/sec. It has been used a helix with a radius of 0.2m for all the cases under the parametric study.

According to the calculations approach mentioned earlier, the time steps for the consolidation process that happens right after the post-installation of the helix into the soil. As well, based on the chosen parametric cases, Table 8.

Tables 9-11 present the calculations of consolidation time steps to the period after ending the installation until finishing the consolidation process. These calculations have been done to 9 cases, which are considering the domain of the helix embedded depth (5m, 10m, 20m) with three conditions of permeability coefficients (5e-7 m/sec, 5e-8 m/sec, 5e-9 m/sec).

Table 8: The parametric study cases.

Embedded Depth (H) = 20 m		
K1 (m/sec)	K2 (m/sec)	K3 (m/sec)
5.00E-07	5.00E-08	5.00E-09

K- Permeability Coefficient (m/sec) = 5e-7		
H1 (m)	H2 (m)	H3 (m)
5.00	10.00	20.00

Table 9: Hand-calculations sheet of the consolidation time steps at embedded depth =5.0m.

Helix Depth= 5 m	5	KB (KN/m2)	1034.09		
S'ov (KN/m2)	32.5	G (KN/m2)	344.70		
S'mean (KN/m2)	22.75	M (KN/m2)	1493.69		

		Duration (Sec)					
		Cv	T				
			0.1	0.3	0.5	1	10
k (m/Sec)	5.00E-07	7.61E-05	53	158	263	525	5254
	5.00E-08	7.61E-06	525	1576	2627	5254	52541
	5.00E-09	7.61E-07	5254	15762	26271	52541	525411

		Duration (Hr)					
		Cv	T				
			0.1	0.3	0.5	1	10
k (m/Sec)	5.00E-07	7.61E-05	0.01	0.04	0.07	0.1459	1.46
	5.00E-08	7.61E-06	0.15	0.44	0.73	1.4595	14.59
	5.00E-09	7.61E-07	1.46	4.38	7.30	14.5948	145.95

Table 10: Hand-calculations sheet of the consolidation time steps at embedded depth =10.0m.

	Helix Depth= 10 m	10		KB (KN/m2)	2068.18		
	S'ov (KN/m2)	65		G (KN/m2)	689.39		
	S'mean (KN/m2)	45.5		M (KN/m2)	2987.37		
		Duration (Sec)					
		Cv	T				
			0.1	0.3	0.5	1	10
k (m/Sec)	5.00E-07	1.52E-04	26	79	131	263	2627
	5.00E-08	1.52E-05	263	788	1314	2627	26271
	5.00E-09	1.52E-06	2627	7881	13135	26271	262706
		Duration (Hr)					
		Cv	T				
			0.1	0.3	0.5	1	10
k (m/Sec)	5.00E-07	1.52E-04	0.01	0.02	0.04	0.0730	0.73
	5.00E-08	1.52E-05	0.07	0.22	0.36	0.7297	7.30
	5.00E-09	1.52E-06	0.73	2.19	3.65	7.2974	72.97

Table 11: Hand-calculations sheet of the consolidation time steps at embedded depth =20.0m.

	Helix Depth= 20 m	20		KB (KN/m2)	4136.36		
	S'ov (KN/m2)	130		G (KN/m2)	1378.79		
	S'mean (KN/m2)	91		M (KN/m2)	5974.75		
		Duration (Sec)					
		Cv	T				
			0.1	0.3	0.5	1	10
k (m/Sec)	5.00E-07	3.05E-04	13	39	66	131	1314
	5.00E-08	3.05E-05	131	394	657	1314	13135
	5.00E-09	3.05E-06	1314	3941	6568	13135	131353
		Duration (Hr)					
		Cv	T				
			0.1	0.3	0.5	1	10
k (m/Sec)	k = 5e-7 m/sec	1.99E-05	0.00	0.01	0.02	0.0365	0.36
	k = 5e-8 m/sec	1.99E-06	0.04	0.11	0.18	0.3649	3.65
	k = 5e-9 m/sec	1.99E-07	0.36	1.09	1.82	3.6487	36.49

From the hand-calculations of the consolidation time steps, Figure 38 shows the relationship between the consolidation time in hours *t* with the consolidation time factor *T,* that for the three cases under study for the helix with embedded depths at (5m, 10m, 20m). The calculations have been done for the case of a helix with a radius of 0.2m and soil permeability coefficient of 5e-7

m/sec. As mentioned earlier for the hand calculations of the time steps, the mean stress *P'* has been calculated according to the intact state of the soil. The graph has been marked by the time factor at 10. This refers to the completion of the consolidation process, which is a result of soil disturbance during the installation process. The soil recovers some of its strength, and the amount of strength recovered depends primarily on the soil sensitivity to disturbance.

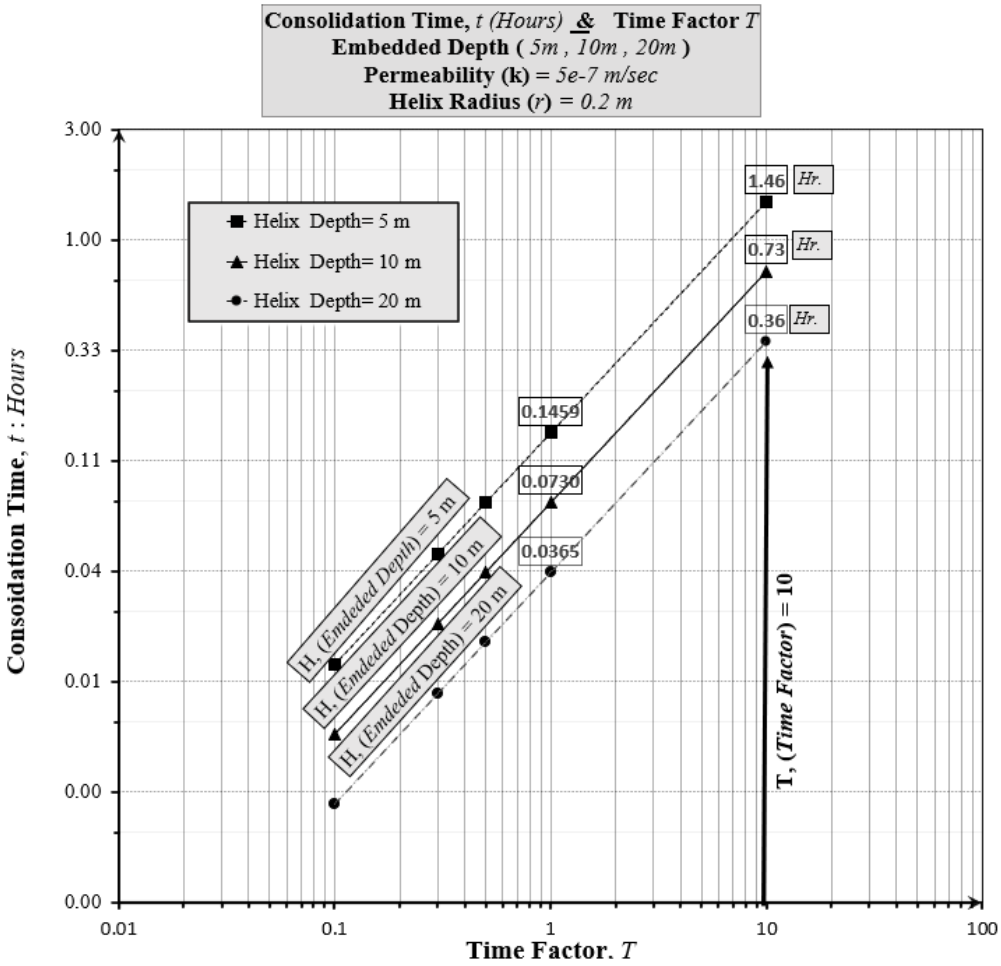

Figure 38: The effect of the helix embedded depth with the consolidation time steps.

.

Figure 39 shows the relationship between the consolidation time *t* in hours with the consolidation time factor *T*. This graph shows the effect of the soil permeability coefficient, which has been examined for the three cases (5e-7 m/sec, 5e-8 m/sec, 5e-9 m/sec). This investigation has been conducted for the case of a helix with an embedded depth of 20m and of a radius 0.2m. It can clearly observe the effect of the soil permeability coefficient between the case of (5e-7 m/sec) and (5e-9 m/sec), which appeared the time needed to end the consolidation process after installation is significantly affected by the soil permeability coefficient.

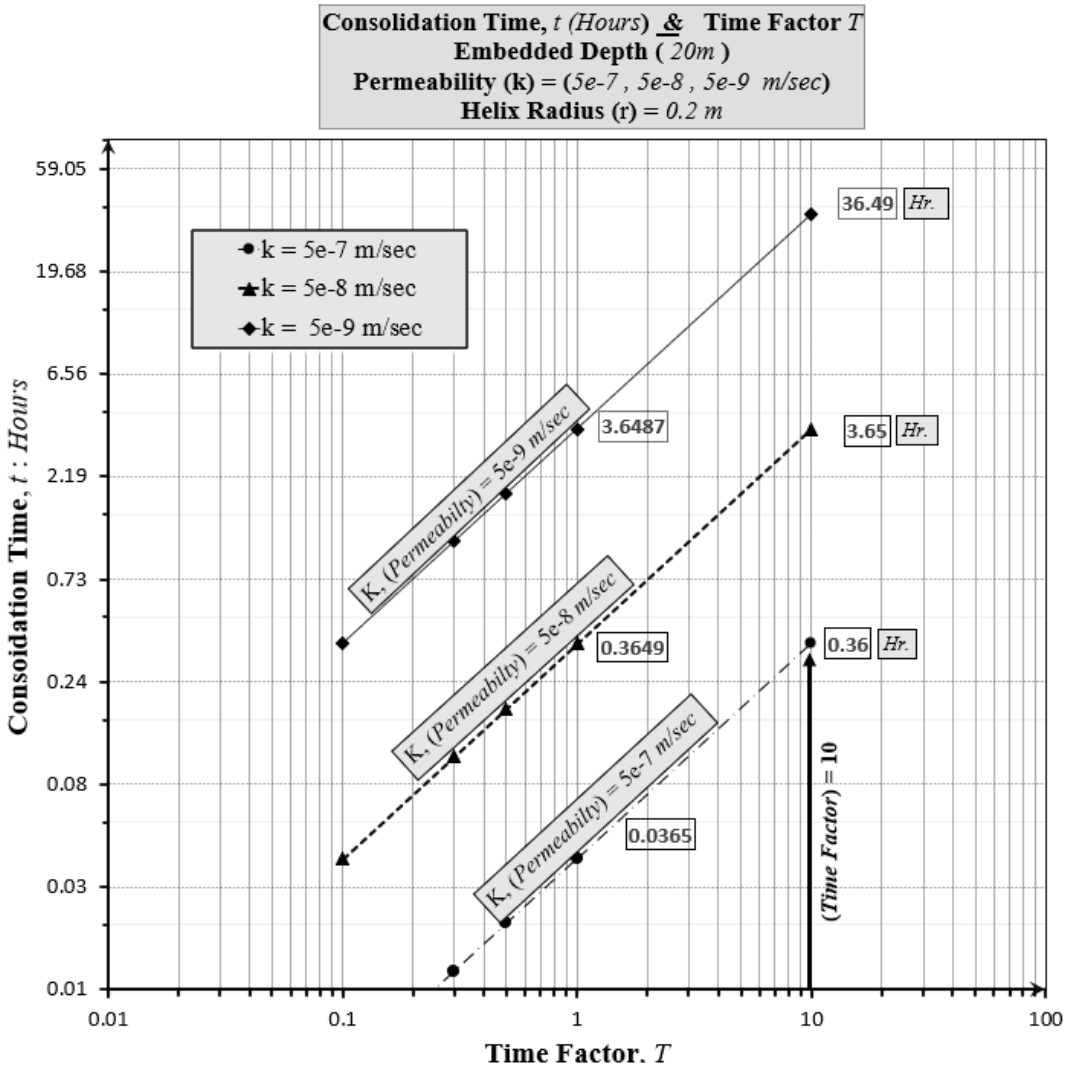

Figure 39: The effect of soil permeability coefficient with the consolidation time steps.

9.6.2 The investigation of excess porewater pressure dissipation and the effective vertical stress after the installation process.

By using the Abaqus, it has investigated the post-installation vertical stress by studying the

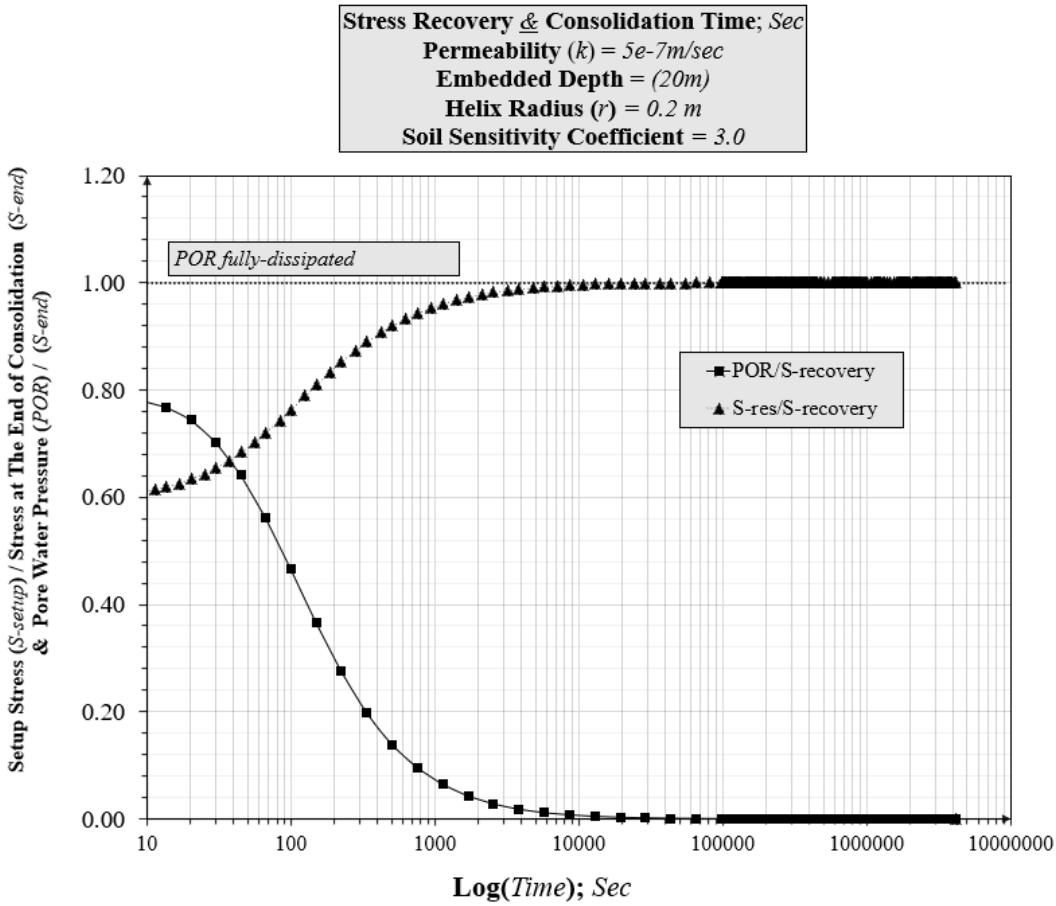

excess porewater pressure dissipation that occurs right after the installation. Figure 40 shows the relationship between the normalized effective vertical stress and the normalized excess porewater pressure as a function of the logarithm of time. The effective vertical stress and the excess porewater pressure are normalized by the value of the effective vertical stress at the end of consolidation. This investigation has been done under consideration of the soil becoming in a disturbed condition after installation with a value of soil sensitivity equal to 3.

Figure 40: The investigation of excess porewater pressure dissipation and the effective vertical stress after the installation process for the case of soil permeability coefficient k =5e-7m/sec, embedded depth H=20m, and Helix radius R = 0.2m.

Regarding the investigation of excess pore water pressure dissipation and the setup-effective vertical stress, Figure 41 shows the dissipation contours of excess porewater pressure starting with the initial condition at the time factor, *T* equal to 0 to the condition of the time factor, *T* equal to 10, which at this stage shows that almost all the excess porewater pressure has been dissipated, and therefore, it can consider this stage as the end of consolidation.

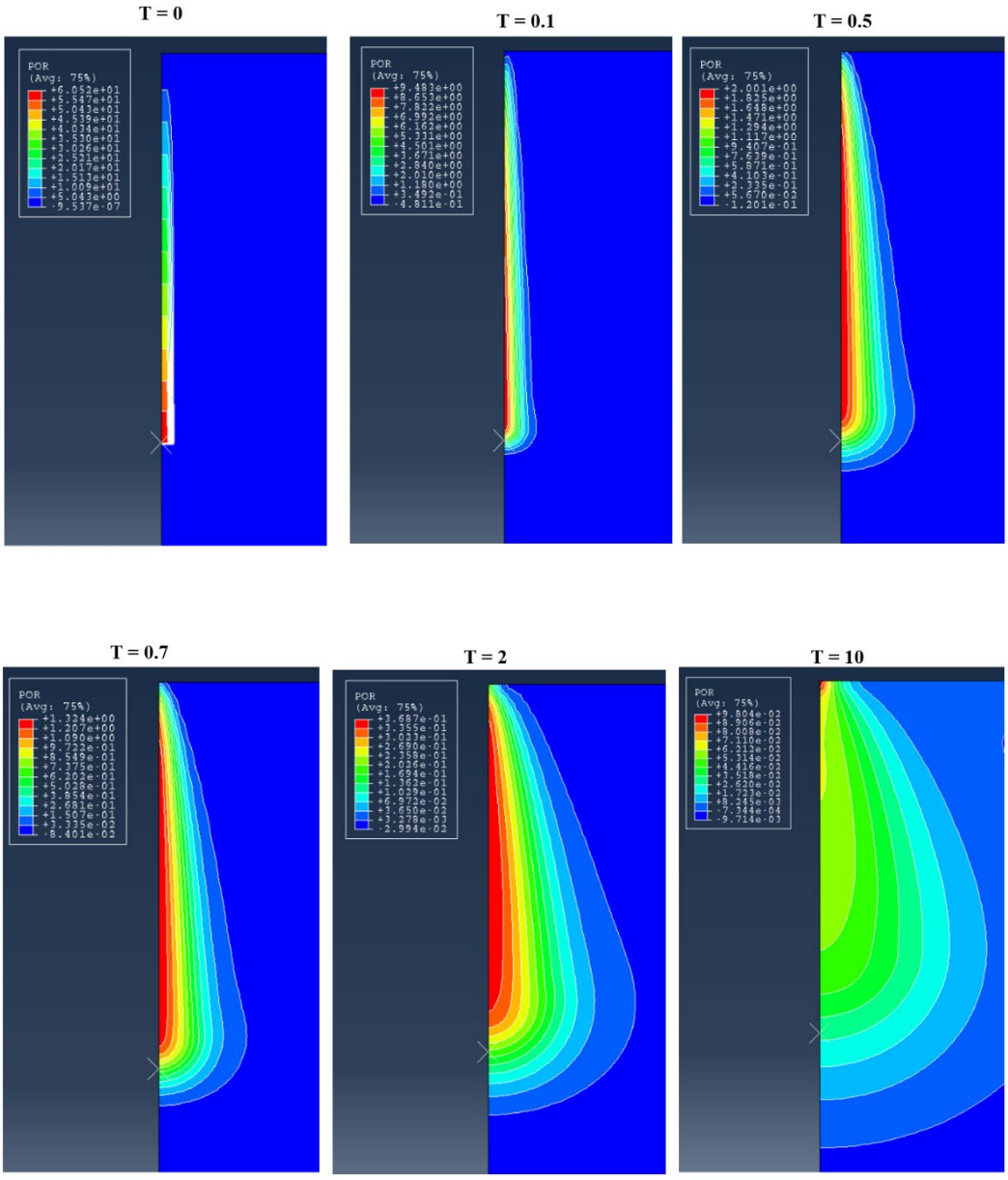

Figure 41: The contours of the excess porewater pressure dissipation of the case of permeability coefficient k =5e-7m/sec , embedded depth H=20m, and Helix radius R= 0.2m.

Due to the helix installation into the soil, the vertical effective stress changes depending on the soil sensitivity factor, which was considered equal to 3 in this examination. Figure 42 shows the effective vertical stress contours for the two states, the first state is immediately after plate installation, and the second state is at the end of consolidation. In addition, that shows the value of the vertical stress recovered at the end of the consolidation, which has been discussed in the next section.

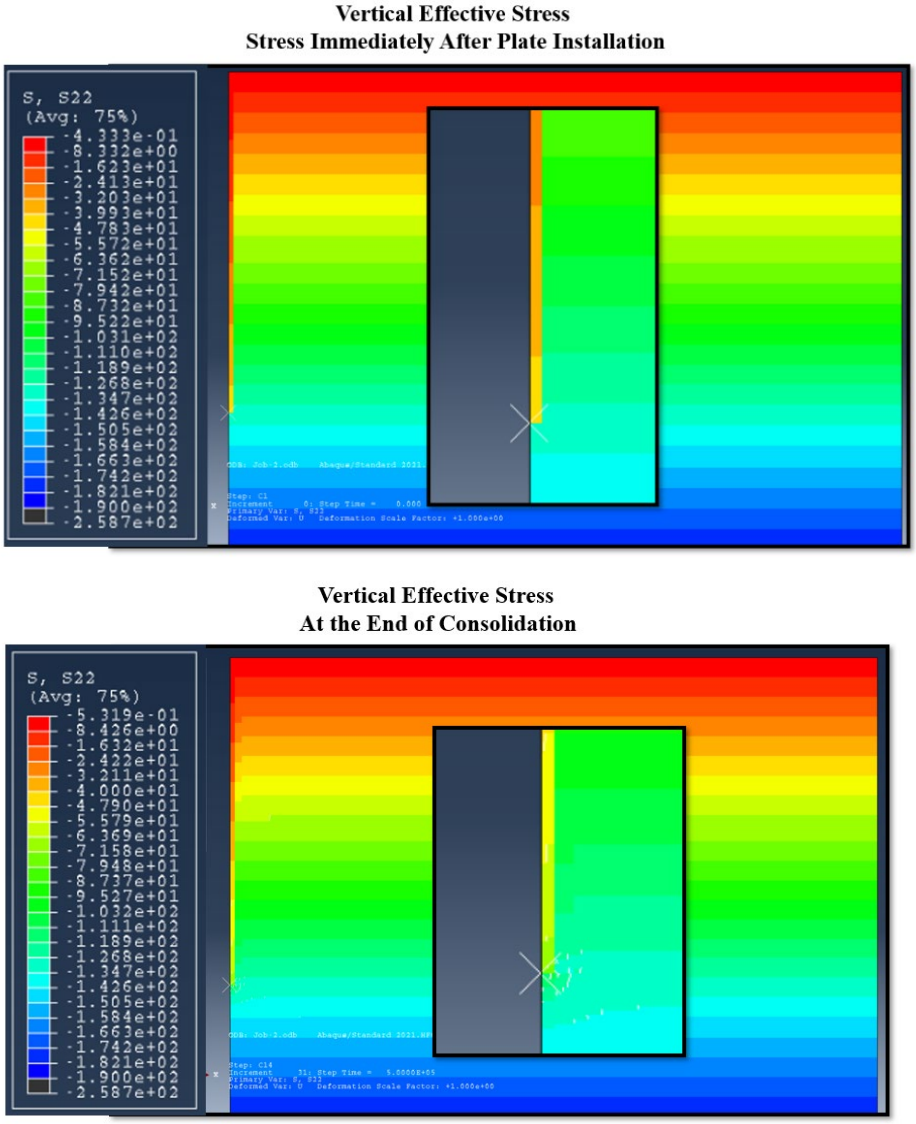

Figure 42: The effective vertical stress contours of the case of permeability coefficient k =5e-7m/sec, embedded depth H=20m, and Helix radius R= 0.2m.
(The initial condition and the condition at the end of consolidation)

9.6.3 The investigation of the setup stress against the changes of permeability coefficient as a function of time.

According to the consideration of soil sensitivity due to the installing process and based on the stress reduction that happens due to that process. It is crucial to investigate the effect of the permeability coefficient, which is the main parameter controlling the consolidation process. In this investigation, the soil sensitivity *St* is considered as 3.0 for the case of the helix with a radius of 0.2m at an embedded depth of 20.0m. The analysis was conducted on three cases of permeability coefficients *k* (5e-7, 5e-8, 5e-9 m/sec).

Figure 43 shows the relationship between the normalized vertical effective setup stress by the initial vertical intact stress as a function of the logarithm of time. The initial intact stress is the stress at the condition before the installation process, that to determine the reduction value in vertical effective stress. It's observed that the installation process has affected the vertical effective stress, where the percentage of the stress immediately after plate installation reaches 33% of the effective vertical intact stress, but eventually with proceeding the consolidation stage, which is mainly a time-dependent process, the percentage of stress at the end of consolidation reaches as a maximum 53.61 % of the effective vertical intact stress.

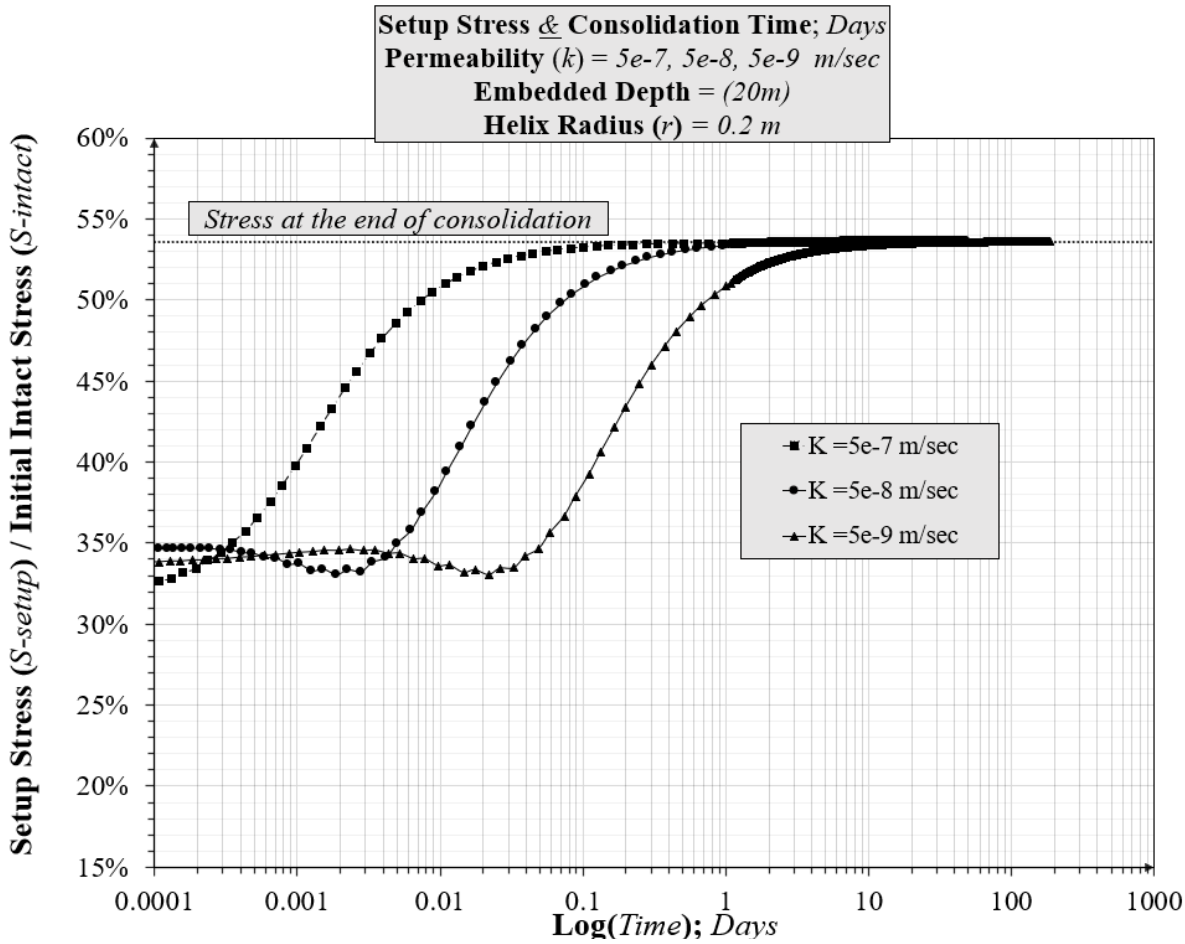

Figure 43: The investigation of the setup stress against the changes of permeability coefficient as a function of time.

9.6.4 The investigation of the setup stress against the changes of helix embedded depth as a function of time.

The embedded depth plays a principal role in rapidly consolidating the soil and recovering the vertical effective stress. Therefore, it has been investigated the effect of the embedded depth in three conditions *H* (5m, 10m, 20m). This investigation was done for the condition of the helix with a radius of 0.2m and a soil permeability coefficient of 5e-7 m/sec. Figure 44 show the relationship between the normalized effective vertical setup stress by the initial vertical intact stress as a function of the logarithm of time. Due to the consolidation process, the percentage of recovered stress reaches a maximum of 53.61 % of the effective vertical intact stress.

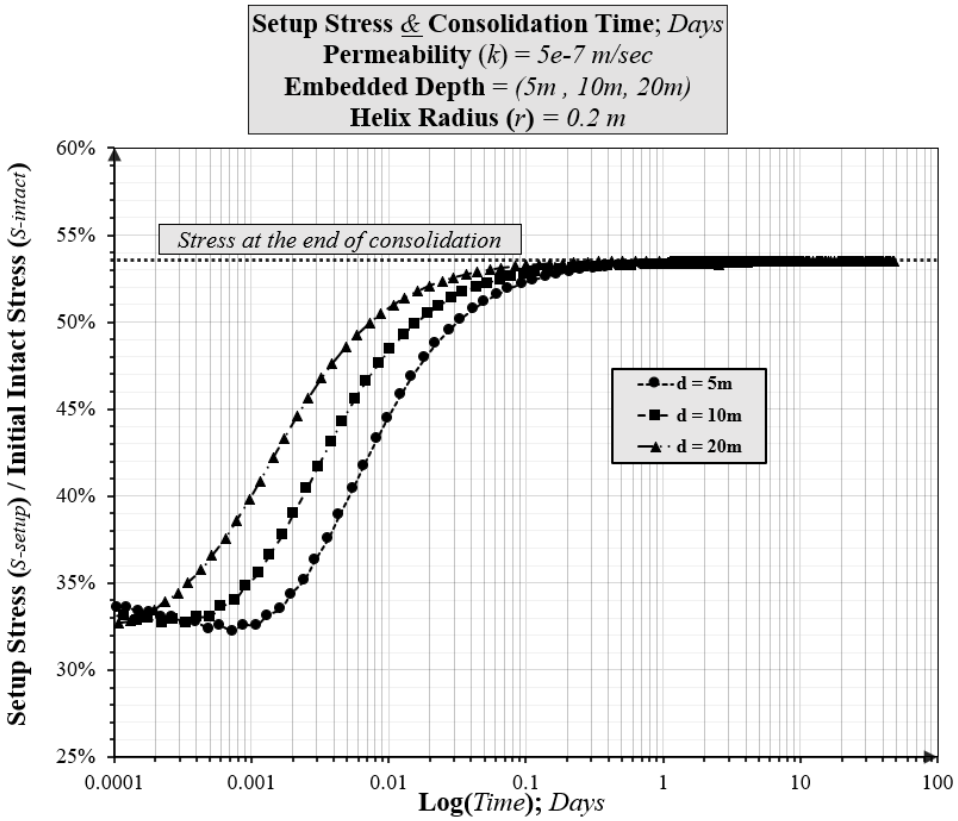

Figure 44: The investigation of the setup stress against the changes of helix embedded depth as a function of time.

9.6.5 A summary of the stress recovery for each of the six cases in the parametric study.

Table 12 Shows the values of the effective vertical stress for three states of the soil due to the installation process. The first state is before installation when the soil is in intact condition. The second state is immediately after plate installation when the vertical effective stress is at its lowest value of it. The third state is at the end of the consolidation process when the soil gets recovered some of its vertical effective stress. The results shown in Table 12 are based on the assumption that *St (*3.0). Moreover, the factor of safety (FOS) for the helix capacity can be determined by the results shown in Figure 47 based on the effect of disturbance soil on the pullout capacity.

Table 12: The Summary of the vertical effective stress at the end of the consolidation.

H (m)	k (m/sec)	Intact Vr. Stress (kN/m2)	Post-installation Vr. Stress (kN/m2)	Stress at The End of Consolidation (kN/m2)	Final Vr. Stress/ Intact Vr. Stress (%)
20	5.00E-07	128.7	42.9	68.99	53.61%
10		63.69	21.23	33.95	53.31%
5		32.4	10.8	17.36	53.58%

H (m)	k (m/sec)	Intact Vr. Stress (kN/m2)	Post-installation Vr. Stress (kN/m2)	Stress at The End of Consolidation (kN/m2)	Final Vr. Stress/ Intact Vr. Stress (%)
20	5.00E-07	128.7	42.9	68.99	53.61%
	5.00E-08	128.7	42.9	68.99	53.61%
	5.00E-09	128.7	42.9	68.99	53.61%

9.6.6 Observation the dissipation time of the pore water pressure under (*St* = 2 & 3).

The determination of the setup stress mainly depends on the assumption of soil sensitivity, it also has the main effect on the dissipation time of the pore water pressure. Therefore, the current study investigated the effect of soil sensitivity on the time of stress recovery. Figure 45 shows the relationship between the normalized effective vertical stress and the normalized excess porewater pressure as a function of the logarithm of time. The effective vertical stress and the excess porewater pressure are normalized by the value of the effective vertical stress at the end of consolidation. This examination was conducted on two cases of soil sensitivity *St* (2.0 & 3.0).

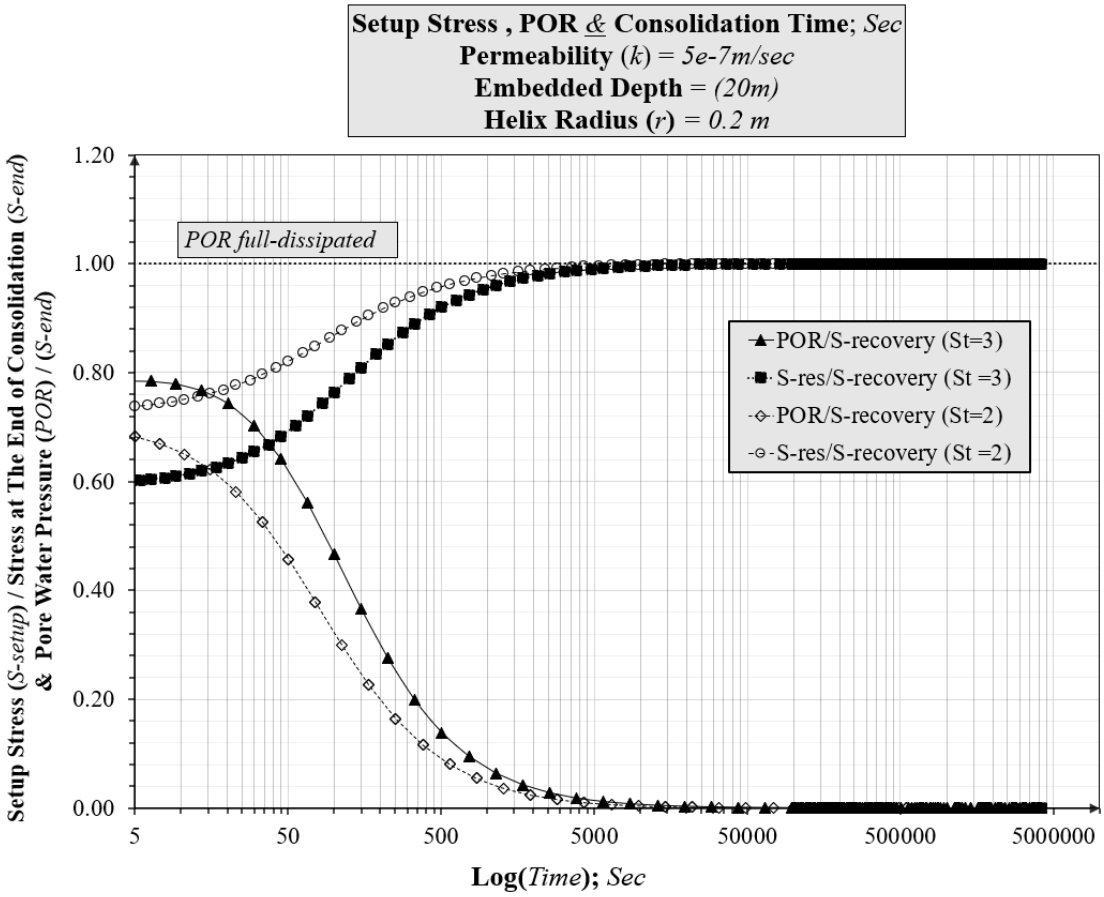

Figure 45: Observation the dissipation time of the pore water pressure under St = 2 & 3.

9.6.7 Observation the stress recovery percentage under (St = 2 & 3).

As mentioned in the previous section about the effect of soil sensitivity on stress recovery at the end of the consolidation stage. Figure 46 presents the percentage values of the setup stress starting with the stage immediately after plate installation until reaching the stage at the end of consolidation. This investigation mainly aimed to obtain the effect of soil sensitivity assumption. The shown relationship is between the normalized effective vertical setup stress by the effective vertical intact stress as a function of time. The study shows significant results, where the soil recovered with a percentage of 53.52% in the case of soil sensitivity of 3.0 and recovered with a percentage of 76.07% in the case of soil sensitivity of 2.0.

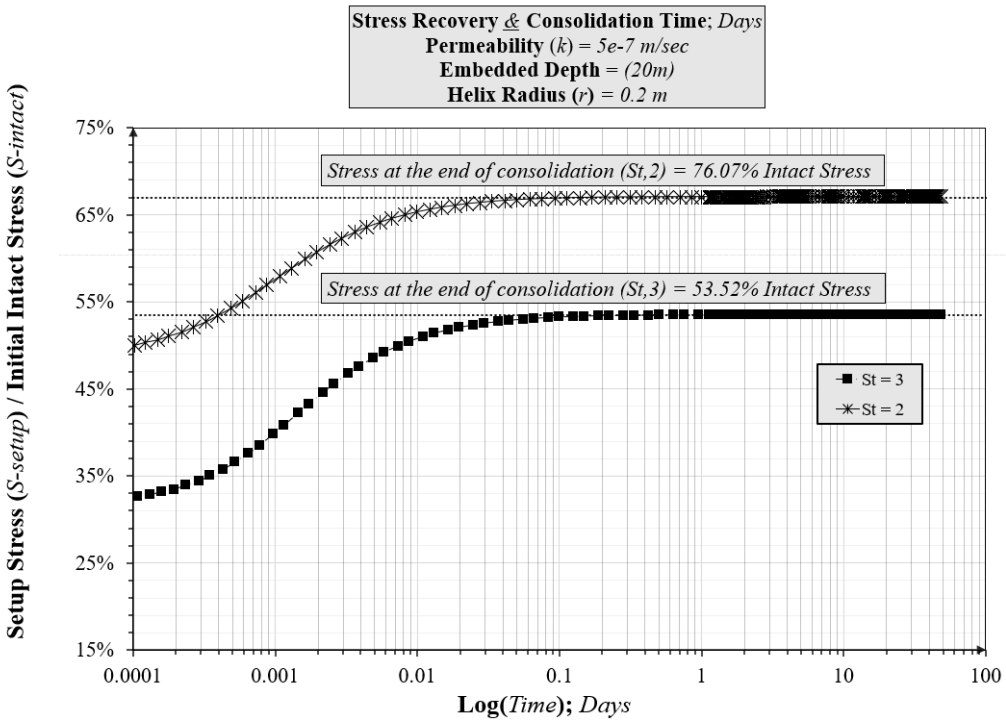

Figure 46: Observation the stress recovery percentage under St = 2 & 3.

9.6.8 Investigation of the Pull-out Capacity with the effect of soil sensitivity.

Ending up with the consolidation process that has been described earlier, and reaching the recovered effective vertical stress, the pull-out stage of the helix comes. Therefore, this investigation was conducted to obtain the pull-out capacity of the helix under a vertical monotonic load. Additionally, due to the effect of the soil sensitivity, it has been analyzed three states at which different soil sensitivity *St* (2.0 & 3.0), and also in a state of intact soil *St* (1.0) to obtain the percentage of capacity drop due to the process of installation. Figure 47.a. shows the relationship of the monotonic pull-out capacity as a function of vertical displacement, while Figure 47.b. displays the normalized pull-out force compared to the ultimate pull-out force at the intact soil state *St* (1.0) as a function of vertical displacement. The analysis was conducted on a helix with a radius of 0.2m, embedded depth of 20m, and a permeability coefficient of 5e-7 m/sec. The results of the study show the effect of soil sensitivity on the pull-out force. When soil sensitivity *St* (3.0)

was applied, it was observed that the soil experienced a loss of about 54% in vertical effective stress, leading to a capacity loss of about 20% for the pull-out force.

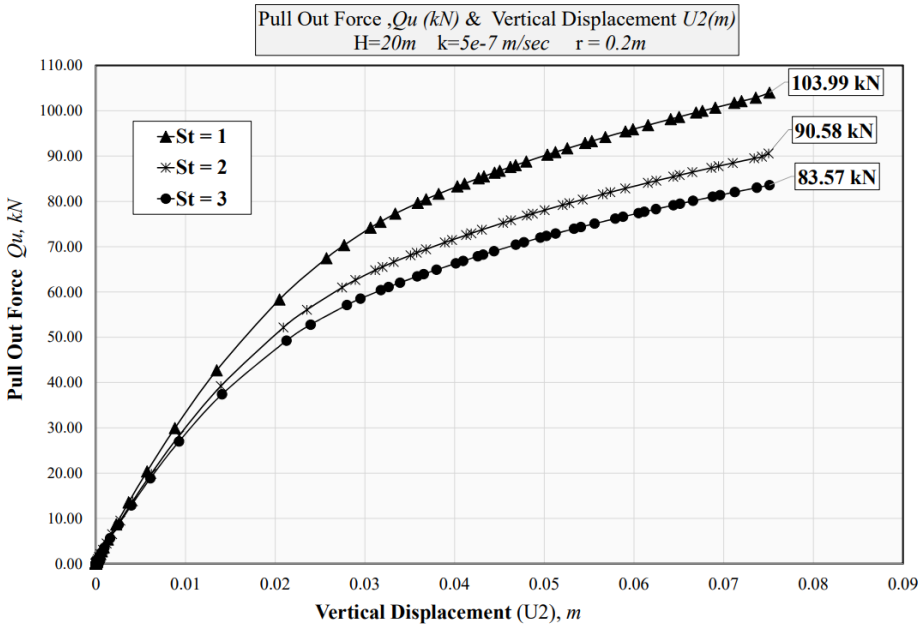

a) Pull Out Force, *Qu (kN)* vs Vertical Displacement, *U2 (m)*

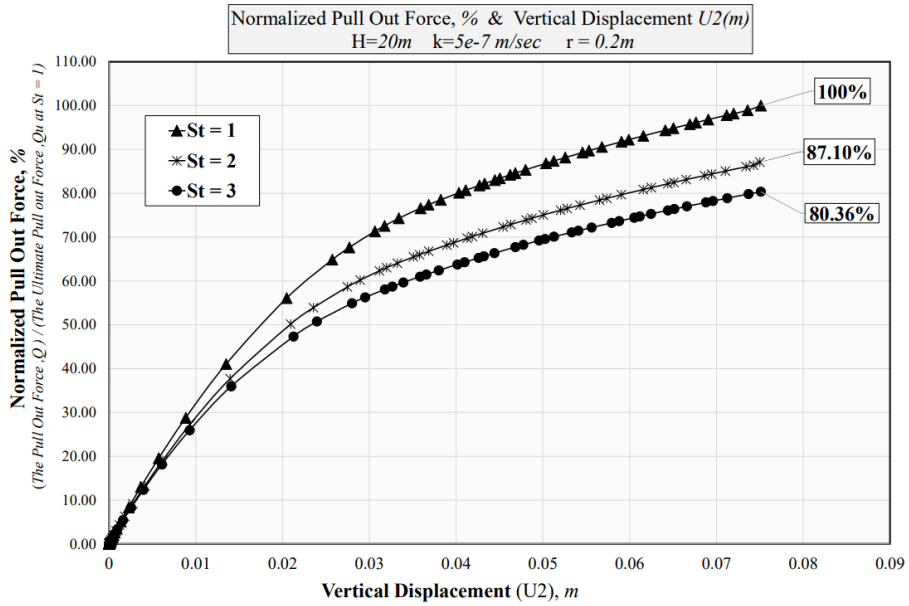

b) Normalized Pull Out Force, *%* vs Vertical Displacement, *U2 (m)*

Figure 47: Investigation of the Pull-out Capacity with the effect of soil sensitivity.

9.6.9 Investigation of the Pull-out Capacity at different embedded depths.

As described earlier in section No. (3.2) about the vital role of embedded depth in the consolidation process. Additionally, it has a high impact on the pull-out capacity under the condition of monotonic load, that is due to the increase of the effective vertical stress. Therefore, the current study has investigated the pull-out force of the helix under a monotonic load for three states of embedded depths (5m, 10m, and 20m). Figure 48.a. illustrates the relationship between the monotonic pull-out capacity and vertical displacement, while Figure 48.b. shows the normalized pull-out force relative to the ultimate pull-out force at an embedded depth of 20 m as a function of vertical displacement. The result demonstrates that increasing the embedded depth significantly increases the maximum helix capacity against the pull-out force. Specifically, the maximum helix capacity is approximately four times greater when the embedded depth is 20 m compared to when it is 5 m.

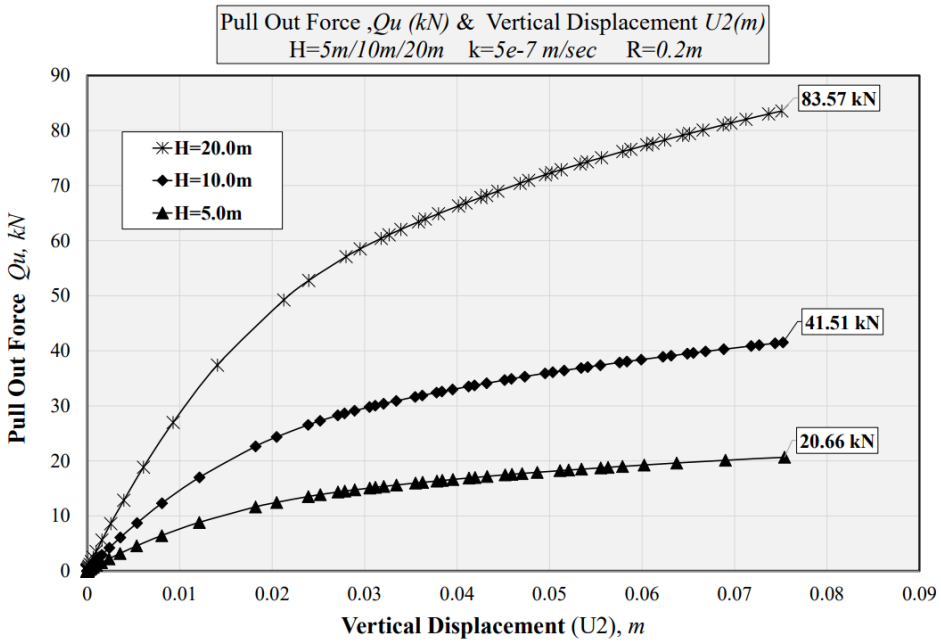

a) Pull Out Force, *Qu (kN)* vs Vertical Displacement, *U2 (m)*

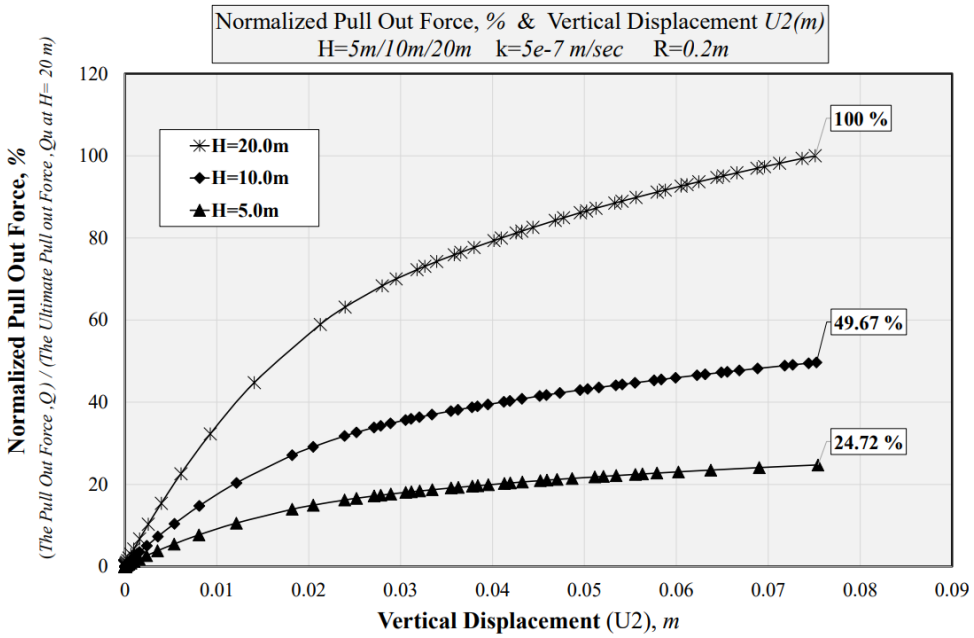

b) Normalized Pull Out Force, *%* vs Vertical Displacement, *U2 (m)*

Figure 48: Investigation of the Pull-out Capacity at different embedded depths.

9.6.10 Investigation the Pull-out Capacity at different Helix Radius.

In order to estimate the effects of plate dimensions on the pull-out capacity at the setup stress, three different plate radii were also considered: r=0.2m, 0.4m, and 0.6m. Since the pull-out capacity can be denoted as the function of the bearing factor (Nc), soil strength at embedment depth (s_u), and plate area ($F=Ncs_uA$), the pull-out capacity at the intact stress can increase linearly with increasing the area of the plate. However, as shown in Figure 49, the increases in the pull-out forces at setup stress are not linear with increasing the plate area. A quadruple increase in the plate area could nearly double the pull-out capacity (r=0.2m vs. r=0.4m). On the other hand, increasing the plate area by a factor of nine would result in a 3.5 times increase in the pull-out force (r=0.2m vs. r=0.4m). A possible explanation for this trend was related to the collapse mechanism of the soil around the plate and setup stress caused by the soil parameters that affect the consolidation process.

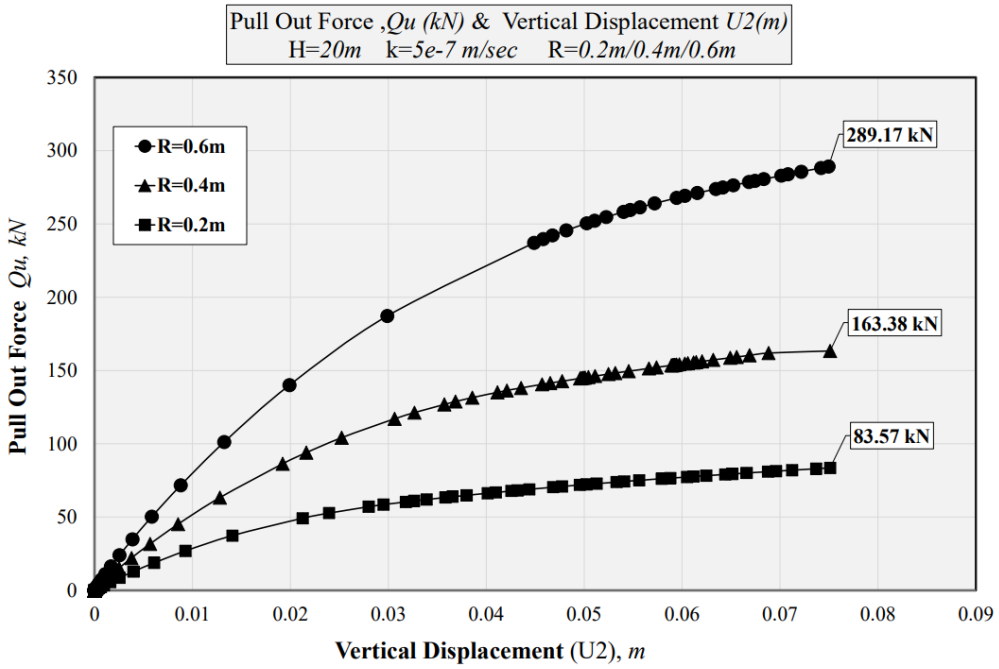

a) Pull Out Force, *Qu (kN)* vs Vertical Displacement, *U2 (m)*

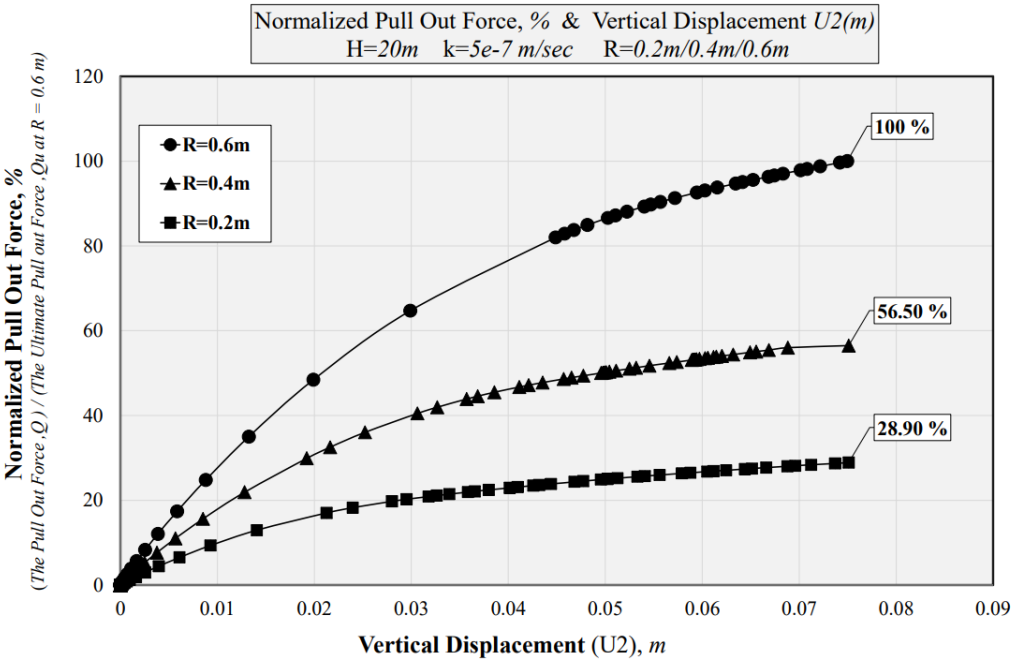

b) Normalized Pull Out Force, *%* vs Vertical Displacement, *U2 (m)*

Figure 49: Investigation the Pull-out Capacity at different Helix Radius.

10. Conclusions

1- Interference effect studies on plate groups indicate that at least three times the diameter of plates can be required as spacing between plates to have the most efficient load capacity for each plate: 24.6 % higher efficiency than two times diameter spacing (Figure 14).

2- Modeling the plate-cable systems as equivalent monotonic springs provides good agreement with a full analysis of a plate embedded in a soil continuum and attached to skirt using a cable. However, equivalent springs are not effective in modeling a cyclically loaded plate-skirt system.

3- Under purely vertical loading, plates increase the ultimate capacity of the HAGIS by about 150% for an aspect ratio of 0.5, and by 60% for the aspect ratio of 1.0. From this perspective, HAGIS is more effective for the smaller aspect ratio (Figures 18-19).

4- For the cases of purely lateral loading considered in this study (Figures 20-22) plates increase the ultimate capacity of the HAGIS by about 10%-30% above that of the skirt by itself.

5- For the cases of inclined loading at a 45° angle considered in this study (Figures 23-25) the simulations indicate that the embedded anchor plates increase the ultimate bearing capacity of the HAGIS by about 50%-140% above that of the skirt by itself.

6- Repeated (N=50) load cycles at one-half the allowable load ($F_{all} = F_{ult}/2$ equal to one-half the ultimate load) produce cumulative displacements on the order of 0.003D (where D is skirt diameter) for a HAGIS described in Section 9.4 subjected to purely vertical cyclic loading (Figure 27).

7- Repeated (N=100) load cycles at one-half the allowable load ($F_{all} = F_{ult}/2$ equal to one-half the ultimate load) produce cumulative displacements on the order of 0.028D (where D is

skirt diameter) for the HAGIS described in Section 9.4 subjected to cyclic loading at a 45° load inclination angle. The horizontal component is about 10 times the vertical component of displacement. That can be explained by the rotation of skirt, where the skirt was loaded at the top of its centerline. This leads to rotating the skirt from the top (not purely skirt translation).

8- Creep simulations indicate that the normalized displacement is about 0.013B (where B is plate diameter) for a sustained load at 50% of the allowable load (Figure 37).

9- Disturbance effect studies showed that effective stress in the zone of disturbance is highly influenced by soil sensitivity. Recovery of effective vertical effective stress following consolidation is on the order 54% to 76% of the initial vertical effective stress, depending on soil sensitivity. (Figure 46).

10- Setup time is dependent on permeability and can be in the range of 0.36 to 36.49 Hours. The effect of disturbance on plate ultimate pullout capacity is also sensitive to plate anchor size and embedment depth. (Figure 39, 47, 48 and 49)

11- Soil sensitivity due to the disturbance that occurs after the installation process, plays a vital role in the capacity of the pull-out force for the system. Based on the analysis done for three cases with different soil sensitivities ranging from 1 to 3, the results in Figure 47 show the drop in capacity that happened when the soil has been disturbed when applying a soil sensitivity equal to 3. The system has lost around 20 % of its capacity against the pull-out force.

12- The study also emphasizes the importance of increasing the embedded depth. As shown in Figure 48, the system capacity increases approximately four times when the embedded depth is 20 m instead of 5 m.

13- According to the investigation of the helix radius, it was found that the helix's capacity against the pull-out force would be increased by approximately 350% when using a helix with a radius of 0.6 meters instead of one with a radius of 0.2 meters. However, the rate of increase in capacity is not constant as the helix radius increases with fixed increment, so it is essential to determine the optimal helix radius for each case based on the necessary capacity.

11. References

Al-Janabi, H. A., & Aubeny, C. P. (2019, July). Experimental Measurement of Thixotropy and Sensitivity in Gulf of Mexico Clay. In The 29th International Ocean and Polar Engineering Conference. International Society of Offshore and Polar Engineers.

Al-Janabi, H. A., Aubeny, C. P., Chen, J., & Luo, M. (2019, April). Experimental Measurement of Touchdown Zone Stiffness for SCR in Gulf of Mexico Clay. In Offshore Technology Conference. Offshore Technology Conference.

Al-Janabi, H. A., Aubeny, C. P., Chen, J., & Luo, M. (2020). Experimental measurement of monotonic and cyclic lateral resistance of risers and pipelines in Gulf of Mexico clays. Canadian Geotechnical Journal, 57(10), 1534-1549. https://doi.org/10.1139/cgj-2019-0410

Al-Janabi, H. A., Aubeny, C. P., & Chen, J. (2021). Cyclically loaded risers and pipelines in cohesive soil. Ocean Engineering, 241, 110056. https://doi.org/10.1016/j.oceaneng.2021.110056

Al-Janabi, H. A., & Aubeny, C. P. (2022). Experimental and Numerical Investigation of the Performance of Piles and Suction Caissons Subjected to Inclined Cyclic Loading in Cohesive Soils. *Journal of Geotechnical and Geoenvironmental Engineering*, *148*(6), 04022036.

Anastasopoulos, I., Gelagoti, F., Kourkoulis, R., & Gazetas, G. (2011). Simplified constitutive model for simulation of cyclic response of shallow foundations: validation against laboratory tests. Journal of Geotechnical and Geoenvironmental Engineering, 137(12), 1154-1168. https://doi/10.1061/(ASCE)GT.1943-5606.0000534

Andersen, K. H. (2015). Cyclic soil parameters for offshore foundation design. Frontiers in offshore geotechnics III, 5. https://doi.org/10.1201/B18442-4

API (2003). Recommended practice for planning, designing, and constructing fixed offshore.

Aubeny, C. P., Han, S. W., & Murff, J. D. (2003). Inclined load capacity of suction caissons. International Journal for Numerical and Analytical Methods in Geomechanics, 27(14), 1235-1254. https://doi.org/10.1002/nag.319

Aubeny, C. P., Murf, J. D., & Moon, S. K. (2001). Lateral undrained resistance of suction caisson anchors. International Journal of Offshore and Polar Engineering, 11(03).

Aubeny, C., & Murff, J. D. (2003). Simplified limit solutions for undrained capacity of suction anchors. In Deepwater Mooring Systems: Concepts, Design, Analysis, and Materials (pp. 76-90).

Chen, W.-F. (1975). Limit analysis and soil plasticity. Amsterdam, Netherlands: Elsevier Scientific Pub. Co.

Helwany, S. (2007). Applied Soil Mechanics: With ABAQUS Applications. Applied Soil Mechanics: With ABAQUS Applications, 1–385. https://doi.org/10.1002/9780470168097

Ho, I. H., & Hsieh, C. C. (2013). Numerical Modeling for Undrained Shear Strength of Clays Subjected to Different Plasticity Indexes. Journal of GeoEngineering, 8(3), 91–100. https://doi.org/10.6310/JOG.2013.8(3).3

Jeanjean, P. (2006). Setup characteristics of suction anchors for soft Gulf of Mexico clays: Experience from field installation and retrieval. In Offshore Technology Conference.

Koros, W., O'Sullivan, M., Pogacnik, J., O'Sullivan, J., & Ryan, G. (2014). Coupled one-dimensional subsidence modelling using elastic-plastic rheology.

Merifield, R. S. (2011). Ultimate uplift capacity of multiplate helical type anchors in clay. *Journal of geotechnical and geoenvironmental engineering*, 137(7), 704-716.

Merifield, R. S., Lyamin, A. V., Sloan, S. W., & Yu, H. S. (2003). Three-dimensional lower bound solutions for stability of plate anchors in clay. *Journal of geotechnical and geoenvironmental engineering*, 129(3), 243-253.

Murff, J., Randolph, M., Elkhatib, S., Kolk, H., Ruinen, R., Strom, P., and Thorne, C. (2005). "Vertically loaded plate anchors for deepwater applications." Proc., Proc Int Symp on Frontiers in Offshore Geotechnics, 31-48.

Randolph, M. F., O'Neill, M. P., Stewart, D. P., & Erbrich, C. (1998). Performance of suction anchors in fine-grained calcareous soils. In *Offshore technology conference*. OnePetro.

Roscoe, K., & Burland, J. (1968). On the generalized stress-strain behaviour of wet clay. https://trid.trb.org/view/124868

Simulia (2014). "ABAQUS Documentation." Dassault Systèmes, Providence, RI, USA.

Sparrevik, P. (2002, January). Suction pile technology and installation in deep waters. In Offshore Technology Conference.

Swain, A., & Ghosh, P. (2019). Determination of Viscoelastic Properties of Soil and Prediction of Static and Dynamic Response. *International Journal of Geomechanics*, 19(7), 04019072-1

Wang, D., Merifield, R. S., & Gaudin, C. (2013). Uplift behaviour of helical anchors in clay. *Canadian Geotechnical Journal*, 50(6), 575-584.

Wood, D. M. (1990). Soil Behaviour and Critical State Soil Mechanics. Cambridge University Press. 1–462. https://doi.org/10.1017/CBO9781139878272

Yafrate, N., DeJong, J., DeGroot, D., & Randolph, M. (2009). Evaluation of remolded shear strength and sensitivity of soft clay using full-flow penetrometers. Journal of Geotechnical and Geoenvironmental Engineering, 135(9), 1179-1189.

12. Appendices

12.1 Appendix A

12.1.1 Vertical Loading

Figure A.1. shows the reference points (RPs) related to each plate. These RPs located in the middle of each plate. RP1 and RP2 are located in the middle of the system.RP1 is located at depth of 0.0 m, connected to the skirt, and RP2 is located at depth of 20 m and connected to the plate below the skirt centerline.

Figure A. 2a-b. shows the cumulative displacements for the skirt and the plates individually. The displacement on the skirt is slightly larger than displacements at other plates. This can be due to the cables that connect the plates to the skirt, where these cables displace when applying loads.

The displacements for RP3-RP10 are all equal as shown in Figure A. 2c.

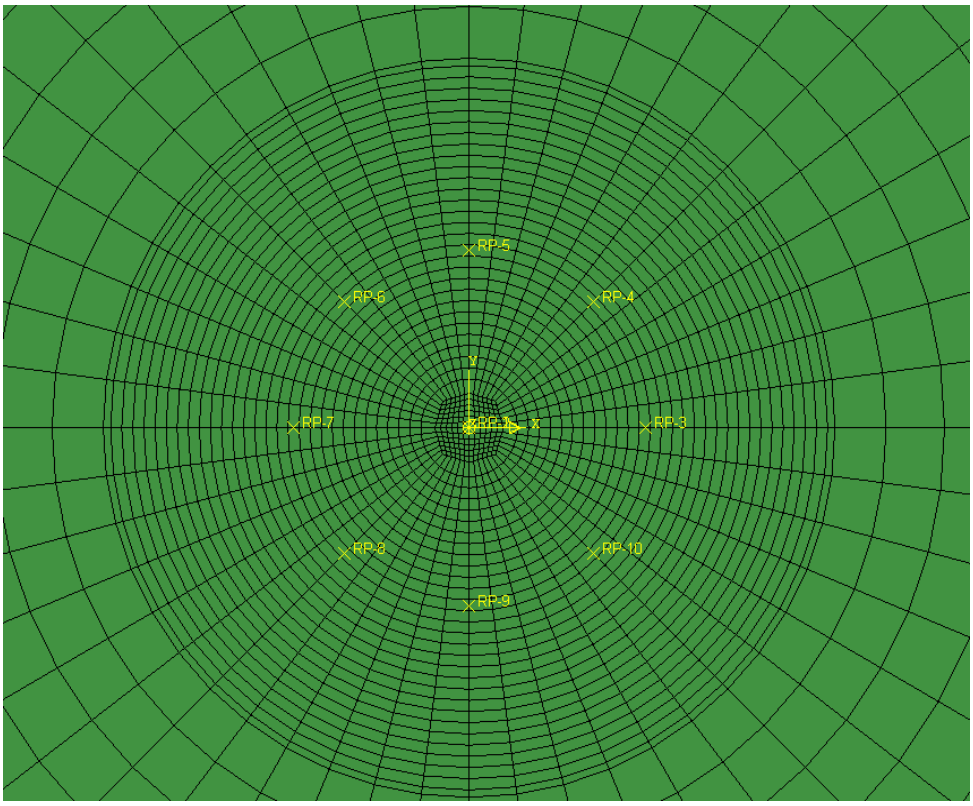

Figure A.1 :Vertical loading with reference points for the plates at 20 m depth.

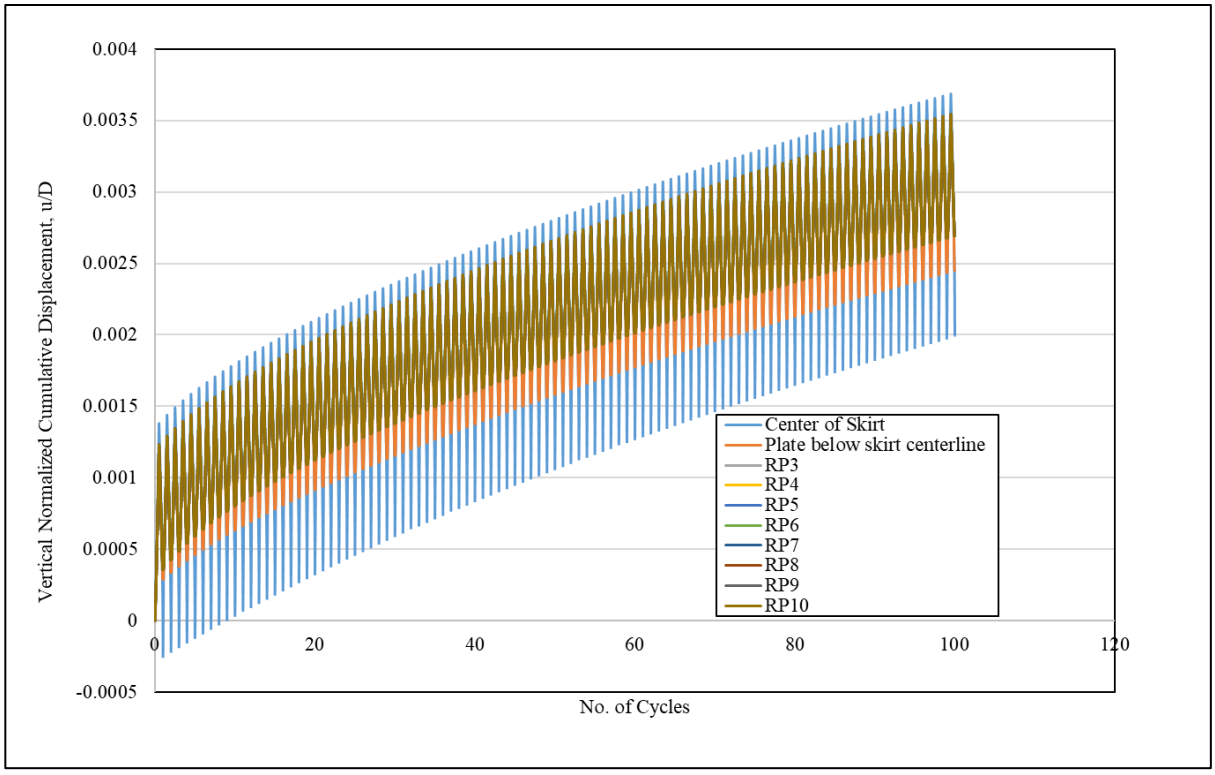

a- Cumulative displacement vs load cycle during purely vertical loading for different plates.

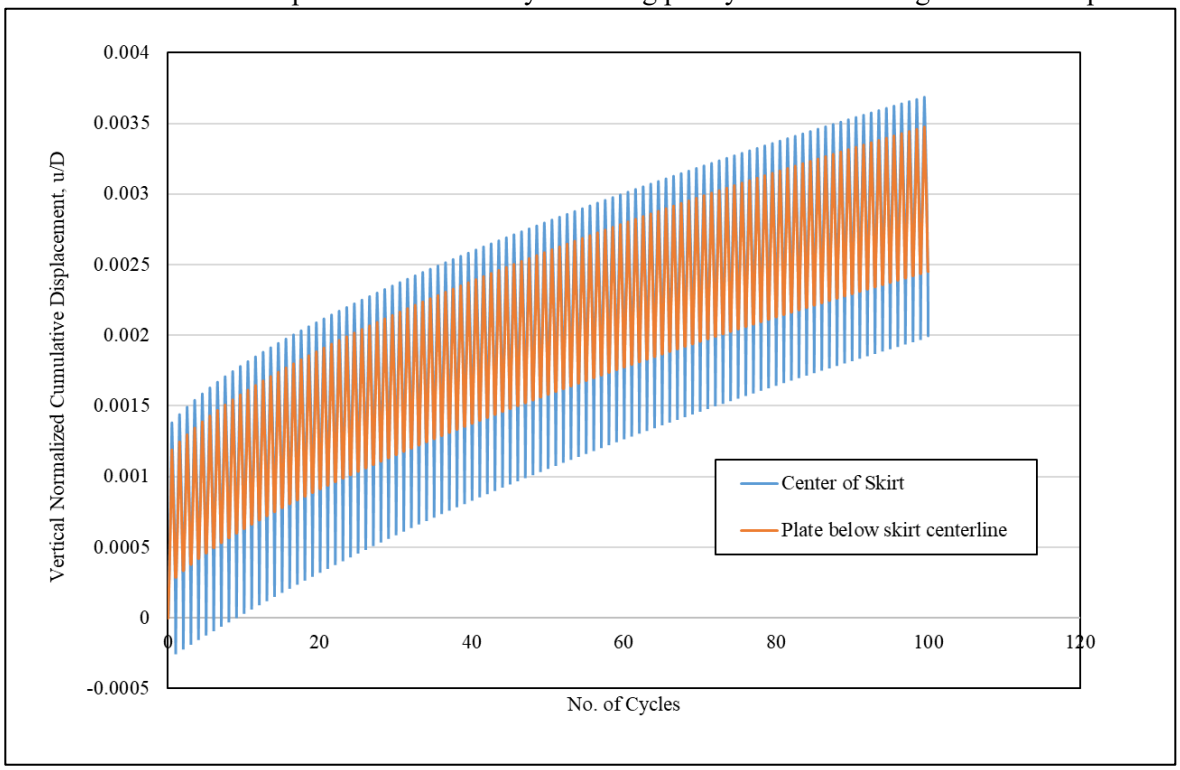

b- Cumulative displacement vs load cycle during purely vertical loading.

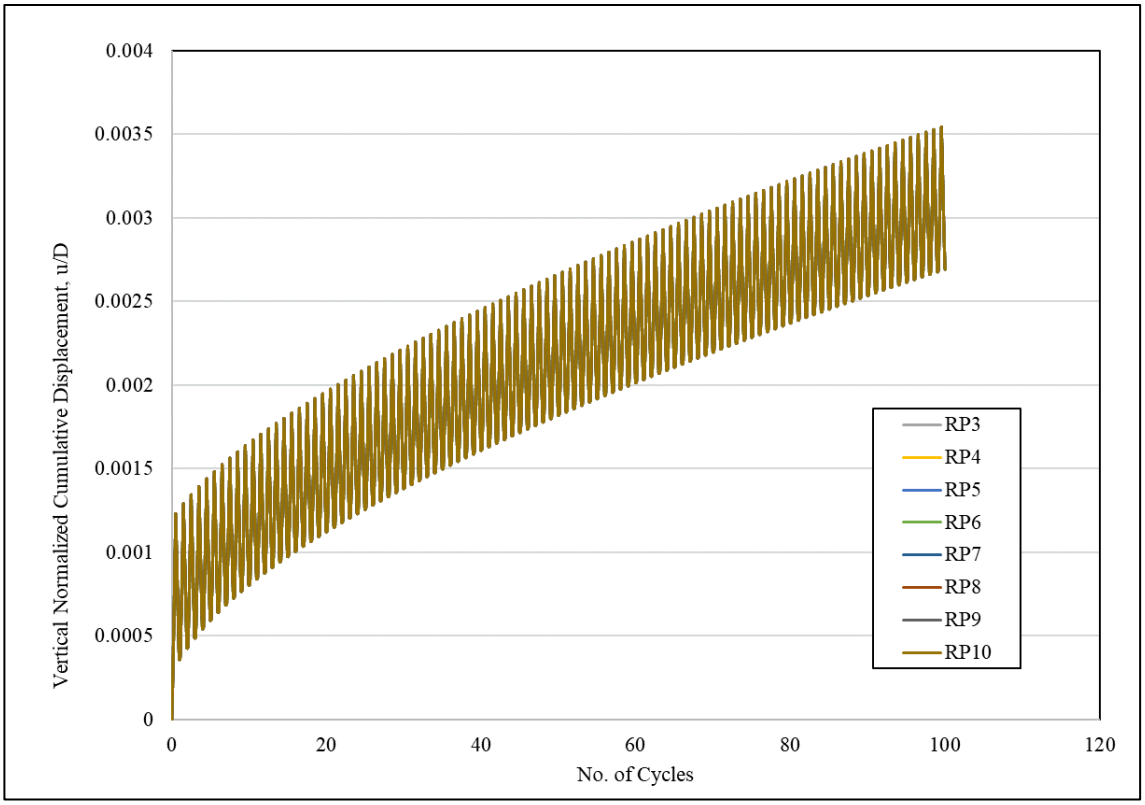

c- Cumulative displacement vs load cycle during purely vertical loading.

Figure A 2 :Vertical normalized cumulative displacements for the skirt and plates.

12.2 Appendix B

12.2.1 Inclined Loading

Figure B. 1. shows the reference points related to each plate. The skirt was loaded from the top at its centerline with a loading angle of 45 degrees.

Figure B. 2a-c. shows the resultant displacements obtained by computing the magnitude of the combined horizontal and vertical components of displacement. Figure B. 2a. shows that the skirt has a higher resultant displacement, and it reduces for the plates depending on the plate's locations. In other words, some plates are subjected to high tension, and some are not (Figure B. 2a-c).

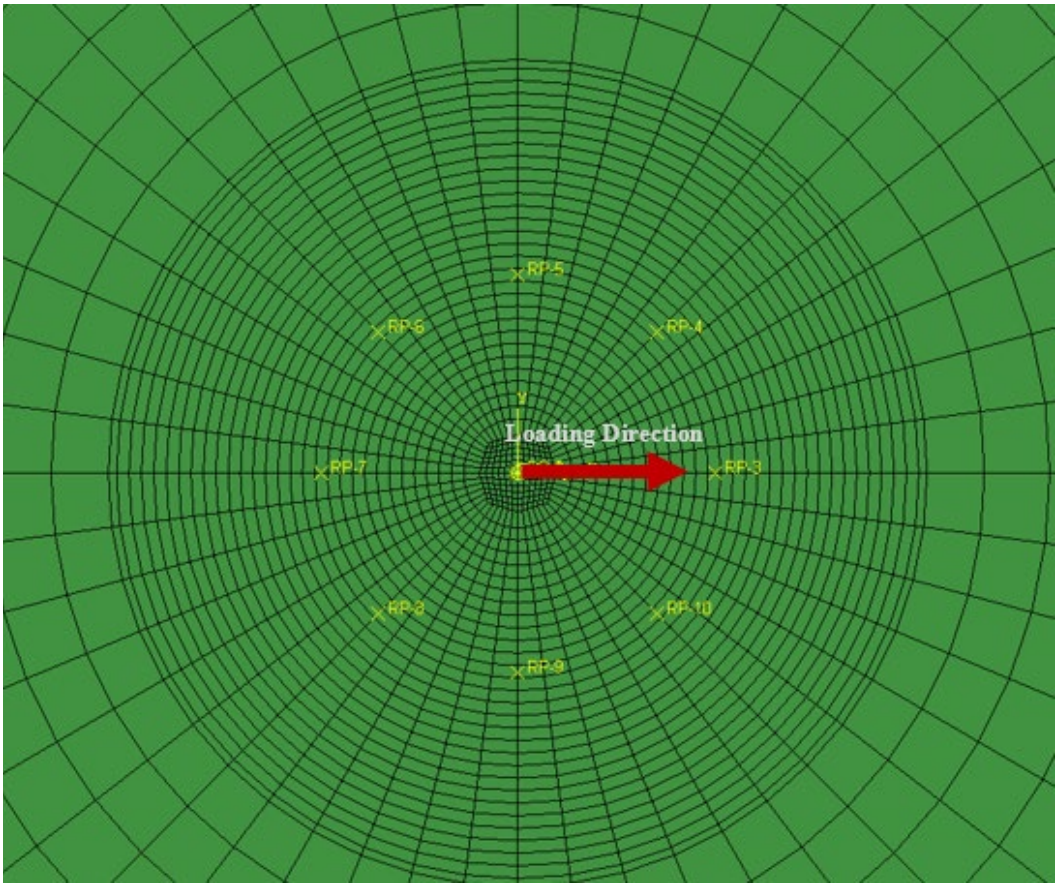

Figure B 1 :Inclined loading (45 degrees) with the plates' reference points

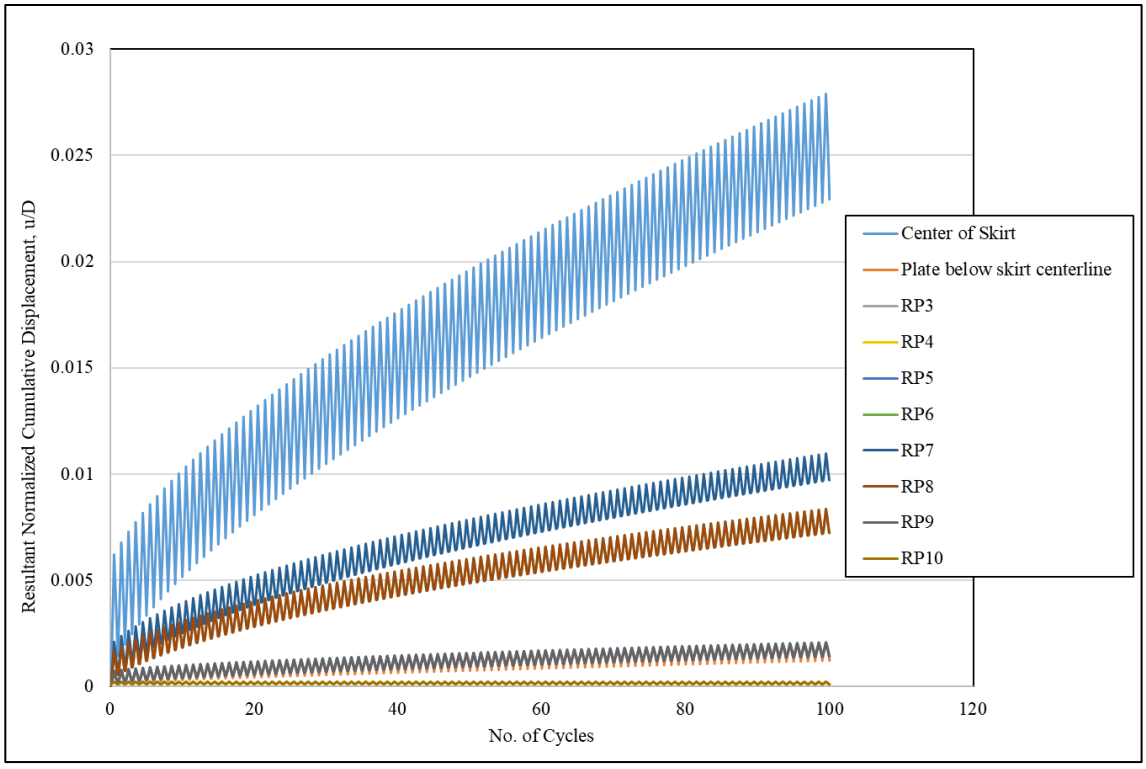

a- Resultant cumulative displacement vs load cycle during inclined loading (45 degrees).

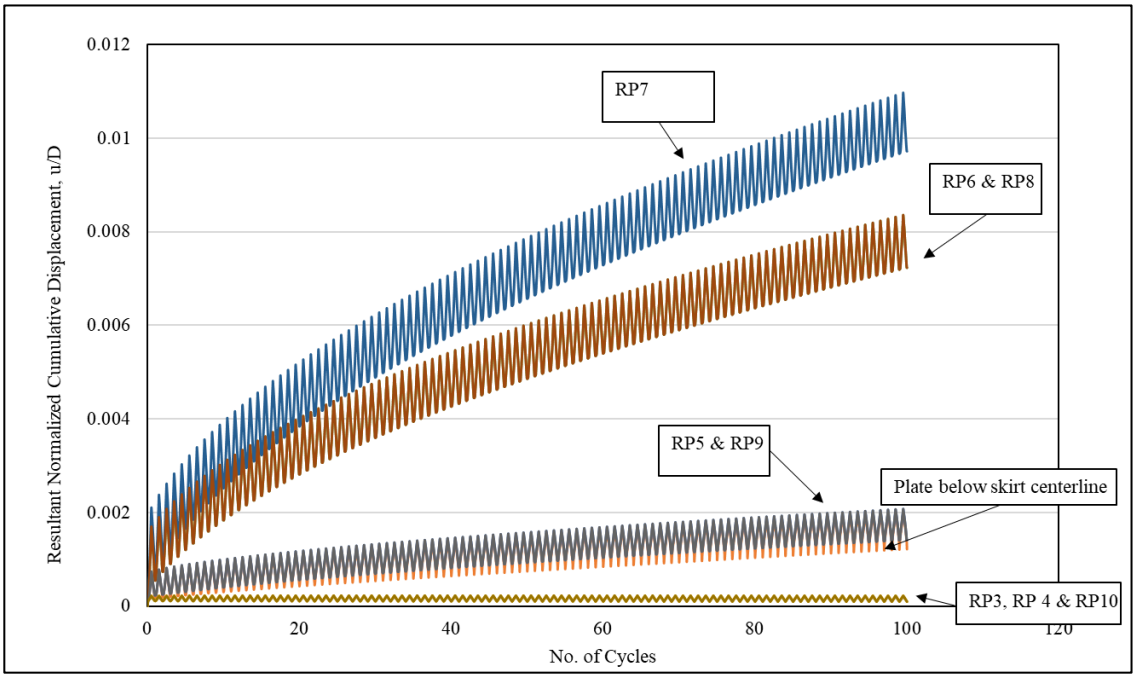

b- Resultant cumulative displacement vs load cycle during inclined loading (45 degrees).

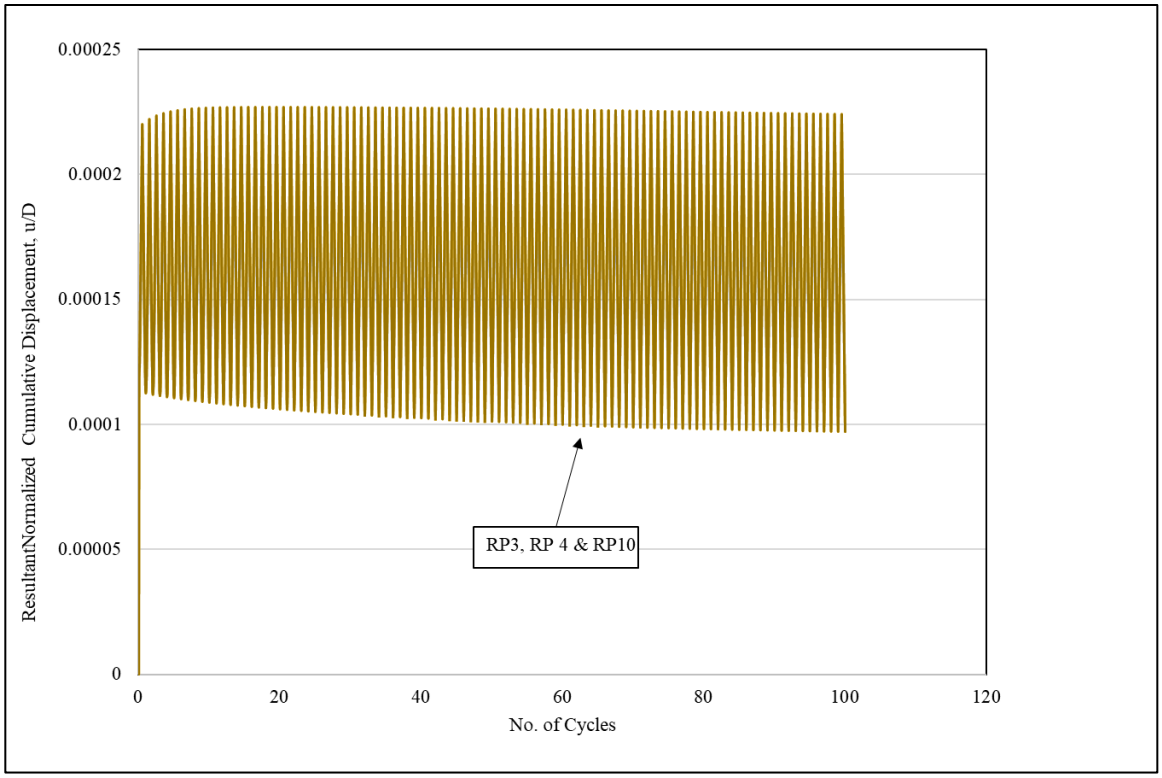

c- Resultant cumulative displacement vs load cycle during inclined loading (45 degrees).

Figure B 2 :Inclined normalized cumulative displacements for the skirt and plates.